



“eLiQuiD”

Best Engineering Training in Electric, Lightweight and Quiet Driving



A European Commission FP7 Marie Skłodowska-Curie
Initial Training Network – European Industrial Doctorate (ITN – EID)
Grant Agreement – 316422

Duration: October 1st, 2012 - September 30th, 2016

Coordination: KU Leuven

Partners: KU Leuven (BE), Virtual Vehicle Research Center (AT), European
Automotive Research Partners Association (BE)

Wim Desmet, Bert Pluymers, Matteo Kirchner

“eLiQuiD”
Best Engineering Training in
Electric, Lightweight and Quiet Driving

**A European Commission FP7 Marie Skłodowska-Curie
Initial Training Network – European Industrial Doctorate (ITN – EID)
Grant Agreement – 316422**

Duration: October 1st, 2012 - September 30th, 2016

Coordination: KU Leuven

**Partners: KU Leuven (BE), Virtual Vehicle Research Center (AT), European
Automotive Research Partners Association (BE)**

Wim Desmet, Bert Pluymers, Matteo Kirchner

© KU Leuven - Departement Werktuigkunde
Celestijnenlaan 300 bus 2420, B-3001 Leuven (Belgium)

Alle rechten voorbehouden. Niets uit deze uitgave mag worden vermenigvuldigd en/of openbaar gemaakt worden door middel van druk, fotokopie, microfilm, elektronisch of op welke andere wijze ook zonder voorafgaande schriftelijke toestemming van de uitgever.

All rights reserved. No part of the publication may be reproduced in any form by print, photoprint, microfilm or any other means without written permission from the publisher.

ISBN 9789073802957
D/2016/5789/2

Preface

Engineering for future mobility must be inspired by ecology and economy to enable green and silent vehicles. Current university based education is focusing on classical fields like mechanical engineering on one side with some aspects of Noise, Vibration & Harshness (NVH) and LightWeight Design (LWD) or like electrical engineering covering aspects of Electrification & Hybridisation (H/E) on the other side.

The eLiQuiD project (Best Engineering Training in Electric, Lightweight and Quiet Driving) aims to bring together early stage researchers and experienced specialists from key players in academia and industry across Europe covering NVH, LWD and H/E disciplines to form a broad range of backgrounds. Recent research underlines the strong interaction and shows the often conflicting demands of these 3 topics.

Consequently, an optimum for future vehicle development requires an interdisciplinary education in this triangle of topics. eLiQuiD's focus is to motivate and encourage early stage researchers for scientific work in the new interdisciplinary research fields NVH+LWD, LDW+H/E and H/E+NVH. The fellows are trained and supported in their phase of doctoral thesis to find innovative PhD topics as well as to receive specific education in theoretical and practical trainings. The education will comprise existing lectures in the partner network as well as training specifically developed for the interdisciplinary needs.

The eLiQuiD consortium is formed by three organizations, combining leading education and research institutions as well as an associated partner well established in European automotive R&D to assist in the dissemination and outreach of the eLiQuiD results. Thus the fellows participate in both the scientific research work and the practical application of new methods of testing and simulation and they profit from extended international knowledge after their academic education when starting to work in the industry.

eLiQuiD was funded by the EC as a Marie Curie European Industrial Doctorate under Grant Agreement 316422 in the Seventh Framework Programme (FP7) and ran over a period of 4 years (October 2012 – September 2016). The project brought together the Katholieke Universiteit Leuven (KU Leuven) as academic partner, Virtual Vehicle Research Center (ViF) as industrial research centre and the European Automotive Research Partners Association (EARPA) as associated partner and together hosted 4 researchers, drawing together skills and expertise in a range of different technical approaches. ViF and EARPA brought specific applications that embed generic difficulties associated with NVH of electrified vehicles, while KU Leuven brought a diverse range of innovative approaches and the capability of research training, provision of courses and dissemination to the wider community. Together the consortium developed and promoted research, knowledge and application of NVH analysis and design techniques within the EU industry.

Near the end of the 4-year eLiQuiD project, each of the 4 Fellows has written a self-

assessment report. This book collects these public domain reports, providing an insight in the theoretical development of each of the approaches studied within eLiQuiD and giving an assessment on their industrial applicability, on open research questions and future challenges. The authors hope that these reports may help others in tackling the substantial challenges still existing in NVH assessment of electrified vehicles.

All people involved in the project would like to express their gratitude towards the EC for the support in the EID eLiQuiD project and the REA (Research Executive Agency) for its continuous support in managing the project. A special word of thanks goes to Lionel Boillot, Sergio Mastropiero, Markus Rester and Olivier Delaunoy, the eLiQuiD Project Officers, and to their colleagues; thank you all for helping us to make eLiQuiD a great success!!

Wim Desmet, Bert Pluymers, Project coordinators
Matteo Kirchner, Early Stage Researcher

List of involved researchers

KU Leuven

Prof. Wim Desmet	Project coordinator, Supervisor
Dr. Bert Pluymers	Project coordinator, Supervisor
Dr. Elke Deckers	Researcher
Dr. Frank Naets	Researcher
Dr. Tommaso Tamarozzi	Researcher
Dr. Stijn Jonckheere	Researcher
Dr. Claus Claeys	Researcher
Ir. Jan Croes	Researcher

Virtual Vehicle Research Center

Dr. Jost Bernasch	Managing Director
Dr. Anton Fuchs	Head of Area NVH & Friction
Ir. Eugène Nijman	Scientific Head of Area NVH & Friction, Supervisor
Dr. Jan Rejlek	Teamleader Vehicle Noise Reduction, Supervisor
Dr. Giorgio Veronesi	Researcher
DI Elmar Böhler	Researcher

EARPA (associated partner)

Dr. Simon Edwards	Chairman
Ir. Margriet van Schijndel-de Nooij	Secretary General
Dr. Bert Pluymers	Chairman TF Noise, Vibration & Harshness
Dr. Aldo Ofenheimer	Secretary TF Materials, Design & Production

Early Stage Researchers (ESRs)

Ir. Vittorio D'Ortona	ESR1
Ir. Matteo Kirchner	ESR2
Ir. Ettore Lappano	ESR3
Ir. Sophie de Rijk	ESR4

Contents

1 NVH analysis and optimisation of lightweight structures	1
1 Executive summary	1
2 Sound transmission testing and analysis of a honeycomb sandwich panel by means of a small cabin	2
2.1 The PMA Soundbox test rig	4
2.2 Sound transmission properties detection	5
2.3 Conclusions	11
3 An inverse approach for the acoustic mobility characterization of a lightweight panel tested in a small reverberant chamber	12
3.1 The patch transfer function (PTF) approach	13
3.2 The bases of the indirect approach	13
3.3 A Numerical application of the methodology	15
3.4 Conclusions	19
REFERENCES	19
2 Cylindrical Nearfield Acoustical Holography	23
1 Executive Summary	23
2 Introduction and general framework	23
3 Cylindrical NAH	24
3.1 Problem formulation and solution regularisation	25
4 NAH with compressive sensing	26
4.1 Problem formulation	26
4.2 Feasibility	28
5 Cylindrical NAH: numerical experiments	31
5.1 Test case	31
5.2 Effects of the regularisation	33
5.3 Simulations	33
6 NAH with compressive sensing: numerical experiments	37
6.1 Test case	38
6.2 Simulations	39
7 Conclusions	40
REFERENCES	42
3 A Parametric Model Order Reduction for simulations of beam-based structures	45
1 Executive summary	45
2 Introduction	46
3 Projection methods for model order reduction	47

4	the reduction scheme	48
5	affine representation for beams	49
	5.1 Axial translation and rotation	50
	5.2 Transverse deflection and rotation	50
	5.3 The affine function	52
6	the greedy algorithm	53
	6.1 A general background	53
	6.2 The proposed greedy algorithm for eigenvector basis	54
7	Study case	55
	7.1 Preprocessing and detailed parametric model generation	56
	7.2 PMOR using the greedy algorithm	57
	7.3 Conclusions	59
	REFERENCES	61
4	Equivalent modelling of sandwich beams	63
1	Executive Summary	63
2	Introduction	63
3	State of the art of sandwich beams dynamics	64
4	Equivalent material model	65
	4.1 Transverse shear stress distribution and correction factors	66
	4.2 Damping	67
5	Analytical performance evaluation	67
6	Experimental study	69
7	General Conclusions	69
	REFERENCES	71

Chapter 1

NVH analysis and optimisation of lightweight structures

VITTORIO D'ORTONA^{1,2,3}, *BERT PLUYMERS*^{2,3}, *EUGÈNE NIJMAN*¹,
WIM DESMET^{2,3}

¹ *VIRTUAL VEHICLE RESEARCH CENTER*

² *KU LEUVEN, DEPARTMENT OF MECHANICAL ENGINEERING*

³ *MEMBER OF FLANDERS MAKE*

1 EXECUTIVE SUMMARY

The use of small reverberant transmission suites, for in-situ Transmission Loss (TL) characterization of panels, has been increasingly implemented in the automotive, railway and aerospace fields in order to have a good knowledge of their vibro-acoustic behaviour and reduce the amount of post-treatments in the sound package of vehicles. Compared to the standards (chambers of 80 m³), the dimensions of these chambers allow for building own designed testrig, resulting to be practical and fast tools for testing and evaluating the vibro-acoustic behavior of lightweight panels of common use in the transport industry.

Nevertheless, there is a wide frequency range in which the acoustic field inside the cabin cannot be considered diffuse. The Schroeder's frequency is high, and below it a strong vibro-acoustic coupling between the sample and the reverberant acoustic environment might be present. The achieved noise reduction properties are then affected by the test rig in which they are measured and cannot be considered as representative for the tested panel's behavior. The lack of diffusivity is a common issue for small cabins and, before diffusivity is reached, it does not allow for a Transmission Loss (TL) investigations that can be comparable with the one measured via a standard procedure. This issue can be circumvented by using an indirect approach aimed at retrieving first the acoustic mobility of the sample unaffactively from the acoustic environment in which it is tested, and then numerically predict its response under the desired acoustic field (e.g. diffuse field, normal incident pressure field, etc).

The first part of the chapter introduces the PMA Soundbox and its main features, together with a test campaign to investigate the Insertion and Transmission Loss properties of a honeycomb sandwich panel. The results show that when the field inside the cavity is not diffuse, a strong vibro-acoustic coupling occurs, affecting the noise reduction properties of the sample.

In the second part instead, the basis and a numerical validation of the indirect approach to overtake the coupling problem is described. For the sake of clarity it is important to mention that both of the sections are based on two conference papers written by the author of this chapter. The first section refers to [1], while the second one to [2].

2 SOUND TRANSMISSION TESTING AND ANALYSIS OF A HONEYCOMB SANDWICH PANEL BY MEANS OF A SMALL CABIN

The application of lightweight structures in the automotive and aviation industries has been increasing to match increasingly ambitious CO₂ emission targets. A recent research shows that lightweight materials already make up 80% of all materials in aviation, and in automotive their use in production will more than double in the next 20 years [3]. The high stiffness to mass ratio of lightweight structures guarantees energy and mass saving, while keeping high mechanical performances. Nevertheless, Noise, Vibration and Harshness (NVH) performances can be unsatisfactory. Post-treatments are then adopted, like for example the addition of visco-elastic layers, reducing the originally expected mass gain. In order to avoid or reduce this side effect, a good a priori knowledge of the vibro-acoustic behavior of lightweight components is needed. Both experimental and numerical tools can efficiently be implemented at this purpose.

Amongst the indicators of the NVH properties, the sound Transmission Loss index (TL) is used to show the acoustic attenuation properties of a given structure in very well defined acoustic environments. The procedure for TL measurements, as well as the entire test rig setup and design, is regulated by international standards (*ASTM Standard E90 04 in 2009*). Normally, the test environment involves chambers with big volumes in order to minimize the interaction between the test rig and the tested sample. In fact, the same specimen tested in different facilities has to theoretically show the same behaviour (as far as each of them fulfils the requirements prescribed in the aforementioned standard).

Typically the test rig consists of two adjacent rooms which can be reverberant or anechoic, allowing for the following combinations:

- two reverberant rooms (diffuse-field incidence and radiation into a reverberant environment, Fig 1.1 on the top-left)
- one reverberant room and one anechoic room (diffuse-field incidence and free-field radiation, Fig 1.1 on the top-right)
- two anechoic rooms (single-incidence and free-field radiation, Fig 1.1 on the bottom-right)
- one anechoic room and one reverberant (single-incidence and radiation into a reverberant environment, Fig 1.1 on the bottom-left).

The test sample - of a minimum dimension of 1.2 m (except for the thickness) - is mounted at the rigid partition wall between the two rooms. In the source room is generated a pressure field that makes the test specimen vibrate. This creates a sound field in the second room. The Sound Pressure Levels (SPL) in both the source and receiving rooms are recorded (*ASTM Standard E90 04 in 2009*) and respectively called $P_{incident}$ and $P_{transmitted}$. The TL comes from Eq. 1.1.

$$TL = 10 * LOG_{10} \left(\frac{P_{incident}}{P_{transmitted}} \right) \quad (1.1)$$

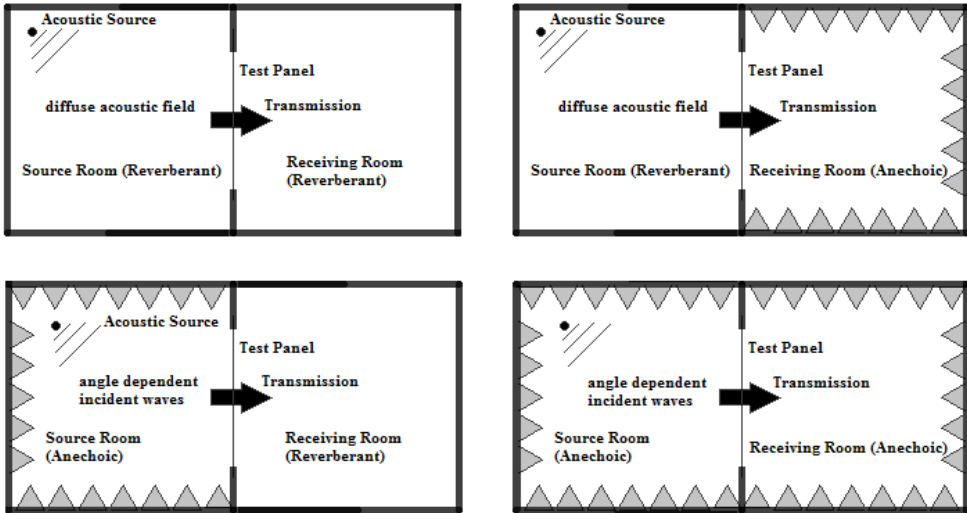


Figure 1.1: On the top-left: two reverberant rooms sound TL suite. On the top-right: a reverberant source room radiating into a free field (anechoic room). On the bottom-left: a single angle incident source (in anechoic room) radiating into a reverberant room. On the bottom-right: a single angle incident source (in anechoic room) radiating into a free field (anechoic room). Lateral view.

Care has to be taken when measuring the pressure field in the reverberant source room, avoiding direct field effects and cavity resonances (satisfying the hypotheses of field diffusivity, i.e. uniform sound pressure level and equally probable flow of energy in all directions). In the case a reverberant receiving room, the same care is also required for the corresponding field acquisitions, and Eq. 1.1 needs to be corrected according to the Sabines formula [4]. Relying on the hypothesis of diffuse field and/or free field, the procedure for noise reduction properties identification is straightforward. Nevertheless, it is worth to point out that the whole facility can be quite demanding and cumbersome. Moreover, the sample dimensions required by the standards can sometimes result not representative of practical application, especially for small and medium sized parts.

With the goal to get a faster and more practical tool for testing and analysing noise reduction properties of lightweight panels of common use in the small sized transport industry, at KU Leuven was designed a new experimental test rig [5]. The facility, named PMA Soundbox, is a small reverberant chamber that supports the research and development of innovative materials and the optimization of lightweight component designs. The PMA Soundbox not only differs from standard facilities in terms of size; compared to them, indeed, it is also a multifunctional test setup which can be used for measuring several NVH parameters, i.e. sound transmission of panels, sound absorption of porous materials, vibration damping and it can also support material properties identification. On the other hand, the experimental test procedure does not rely on simplified field assumptions, a more complex pressure field is present and this has to be taken in account when performing measurements. Hence, in the low frequency region (below field diffusivity), the experimental identifications are supported by numerical modelling techniques able to tackle coupled vibro-acoustic problems, characterized by modally dominated acoustic sub-domains, which are typically encountered in transport industry.

The present section is structured in three main parts. First, the design and technical specifications of the PMA Soundbox are briefly described. The second part reports about the tests carried out for vibro-acoustic studies of the tested panel. These experimental results are compared with numerical simulations. Modal analysis data are used to validate the Finite Element (FE) model of the sandwich plate. This structural numerical model is coupled to a Boundary Element (BE) model of the acoustic cabin, in a fully coupled problem, and the numerical results compared to the experimental measurements. In the last section, the noise reduction performance measured with the PMA Soundbox is compared to the TL evaluated by means of standard facility. Ongoing and upcoming studies, aiming at widening the implementation of the PMA Soundbox in the research field of the vibro-acoustic study of lightweight structures, are finally given in the last section.

2.1 The PMA Soundbox test rig

The design of the PMA Soundbox test rig is based on a preliminary work carried out on a smaller setup [6] and consists of a single cabin. The main advantages of this test rig are:

- It is relatively small (only 0.83 m³), moveable and cheap.
- It allows for several kinds of measurements on components of different sizes and thicknesses in a wide frequency range ([50 – 20000] Hz), for both airborne and structure-borne excitation.
- The test window can be enclosed by a flexible component. In this configuration, the sound Insertion Loss (IL) can be measured.

The IL is defined as the difference in dB between the SPL radiated outside the cabin when an acoustic source is active inside and no specimen is applied to the cabin (this condition is called open-window configuration, and the SPL measured is named P_{open}), and the SPL radiated when the tested component is mounted (P_{closed}).

$$TL = 10 * LOG_{10} \left(\frac{P_{open}}{P_{closed}} \right) \quad (1.2)$$

Unlike the TL, the IL not only depends on the NVH properties of the examined structure but it is also a function of the vibro-acoustic environment in which it is measured, consisting of both the vibrating element and the acoustic cavity. Although the test procedure is not very demanding, care is required in the discussion of the sound transmission characteristics of the test panel, especially in the low frequency region. In fact, till the diffusivity condition inside the chamber is not reached, the modal behaviour of the acoustic subdomain strongly couples to structural one. In view of this, the PMA Soundbox has been designed in order to get a uniform distribution of the natural acoustic frequencies, avoiding overlapping frequencies and uneven gaps between subsequent acoustic natural frequencies. To this purpose, the final design of the test cabin consists of a non-rectangular parallelepiped volume, in which the inner walls are not parallel. The global shape is convex [7]. The simplicity of the geometry and the accuracy of the imposed boundary conditions allow for accurate numerical models, able to satisfactorily predict the observed behaviour over a wide frequency range.

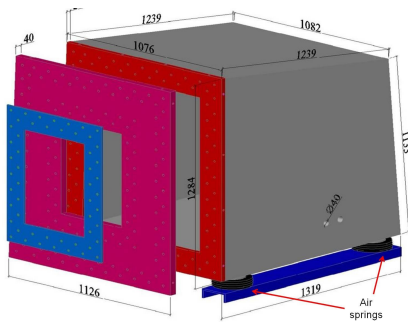
Fig. 1.2 shows the practical realisation of the PMA Soundbox as a five walled reinforced concrete cabin. The cabin can be enclosed at the front side by a modular partition. Test panels

of different thickness and in-plane dimensions can be installed using different front partition walls. All the available front walls are made of aluminium and each of them is 0.035 m thick (see Fig 1.2.a).

The available test partitions are listed below, sorted by the dimension of the test windows:

- A1 window
- A2 window
- 500 mm x 350 mm window
- A3 window
- A4 window
- Fully closed wall

The total weight of the setup is about 3 tons. A three wheels system allows the rig to be moved to the desired location. As visible in Fig. 1.2.a), the PMA Soundbox is suspended on a four air-spring system, required to suppress vibrations coming from the laboratory floor.



(a)



(b)

Figure 1.2: (a) A sketch of the vibro-acoustic test rig; (b) Sound intensity measurements [1].

The setup can be equipped with several sensors for acoustical and structural response acquisitions (PP sound intensity probe, free-field and reverberant-field $\frac{1}{2}$ " microphones, lightweight 1D accelerometers). By means of a full range speaker placed inside the cabin, or of an electro-dynamic shaker, or an impact hammer, both structure-borne and airborne excitations measurements can be performed.

2.2 Sound transmission properties detection

In this section, an aluminium honeycomb core sandwich panel, used for space rocket applications, is described. In order to verify the numerical model of the tested panel, modal analyses in free and clamped edges conditions have been performed. Then, in collaboration with the Japanese Aerospace Agency (JAXA), the noise reduction characteristics have been experimentally and numerically evaluated, by using both the standard test methodology and the PMA Soundbox.

2.2.1 The tested honeycomb sandwich panel

The test specimen is a honeycomb sandwich plate of 11.2 mm total thickness. The core is an AL-3/16-5052T-.001, 10 mm thick with hexagonal regular cells. The top and bottom face sheets are 0.6 mm thick and made out of AL-5052T. A scheme of the plate is represented in Fig. 1.3 and the main geometric dimensions are listed in Table 1.1.

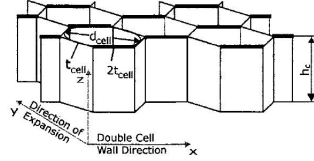


Figure 1.3: Geometric configuration of the core of the tested honeycomb sandwich panel [1].

Geometric properties of the test panel	mm
t_{cell} : wall thickness	0.034
d_{cell} : cell size	4.76
h : core height	10
t_s : surface sheets global thickness	1.2
length along direction of expansion in free edges condition	600
length along double cell wall direction in free edges condition	800

Table 1.1. Geometric properties of the tested honeycomb sandwich panel [1].

2.2.2 Modal Analysis of the specimen

Rowing hammer impact tests have been performed in free and clamped edges conditions. A test grid has been defined in order to capture the modal shapes up to a maximum of half wavelengths equal to 4 along the major edge (chosen as y axis) and 3 along the shorter one (chosen as x axis). The grid is made of 88 input points and three of them have been also used as output points. Three lightweight accelerometers (pcb 352A24) have been placed to measure the acceleration signals at these locations. In free edges condition the panel is suspended using a spring. In free conditions its size is $600 * 800 \text{ mm}^2$. Fig. 1.4 shows the sum of the three measured FRFs up to 1 kHz. In the same figure and the first five experimental modal shapes are also indicated.

When the sandwich panel is tested with clamped edge conditions, the test surface is reduced to an A2 size, e.g. $420 * 594 \text{ mm}^2$. In order to better identify the uncoupled structural natural frequencies of the tested panel, the experimental modal analyses in clamped condition have been performed in two different configurations:

- The isolated system, consisting only of the front wall and the panel clamped at the test window

- The coupled system, having the tested panel clamped to the front wall and mounted on the PMA Soundbox

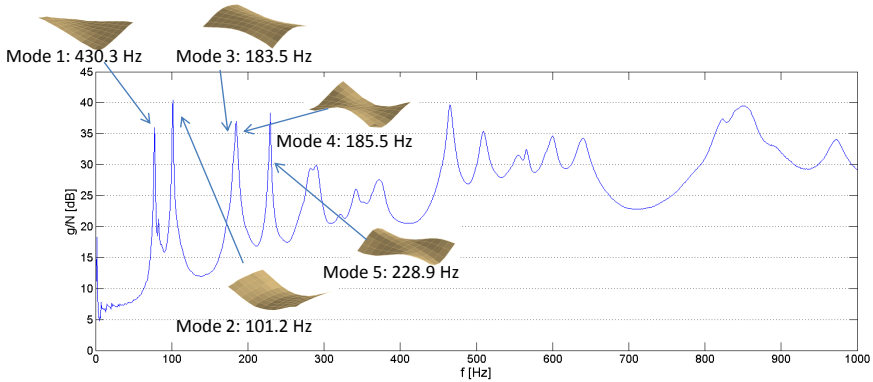


Figure 1.4: Sum of FRFs function recorded on the tested panel (88 points) in free conditions and first five modal shapes [1].

The sums of the FRFs recorded in the two cases are compared in Fig. cite1.5, where the first clamped modes are also shown. Considering the measurements performed for the uncoupled structural system, i.e. with the front wall resting vertically on the floor and the honeycomb panel clamped at its test window, the sum of the FRFs shows the natural frequencies of the clamped panel uneffectively from the presence of the cabin. Some extra peaks related to the modal behaviour of the front wall itself can be also observed. The amplitude of these occurrences is however not comparable to that of the natural modes of the panel itself.

When the front wall is mounted on the Soundbox, the influence of the acoustic subdomain is evident. The acoustic and the structural natural modes couple together and give rise to a multitude of peaks that are visible in the sum of the FRFs. A shift towards higher frequencies of the natural coupled frequencies can be observed compared to the isolated system. The above mentioned shift can be related to the higher stiffness that the system reaches when the front wall is coupled to the cabin.

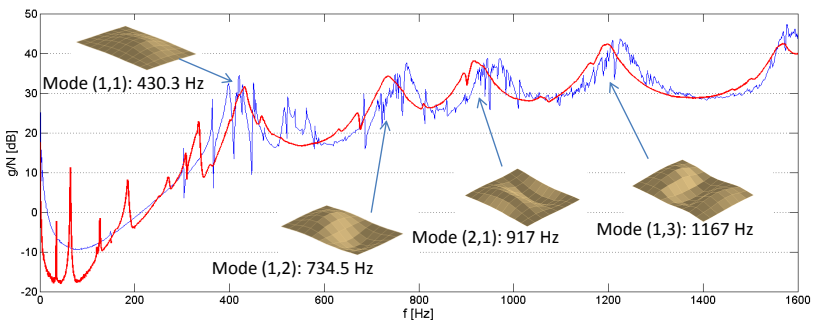


Figure 1.5: Experimental sum of the FRFs function recorded on the tested panel (88 points) clamped to the Soundbox (blue curve) and clamped only to the frame (red curve) [1].

2.2.3 Insertion Loss characterization

The sound IL of the honeycomb panel is measured with the PMA Soundbox. This requires two measurement sets:

- The measurement of the acoustic power radiated outside the cabin when the test window is left empty (open-window configuration)
- The same measurement repeated with the honeycomb panel mounted at the front wall (closed-window)

In both cases, the inner pressure field is excited by a broad range loudspeaker fed by a white noise voltage signal up to 1600 Hz. The speaker is placed at one of the inner corners of the cabin in order to excite all the acoustic modes. The acoustic power radiated outside is obtained from the sound intensity measured over the test area by means of a PP sound intensity probe. The probe scans an area 10 cm far from the tested panel. The sound intensity is measured in 70 points. Each of them corresponds to the centre point of an element of the grid previously used for the modal hammer test with clamped edges condition. The sound intensity detected by the PP probe at each output point is considered to be the averaged value over the corresponding elementary surface (Fig. 1.2.b). The third octave band averaged sound IL is plotted in Fig. 1.6 together with the sound intensity mapping over the acquisition plane in front of the test area at the frequencies of the first modes. Up to 1 kHz the strong modal low frequency behaviour is clearly indicated by the presence of well separated dips in the IL.

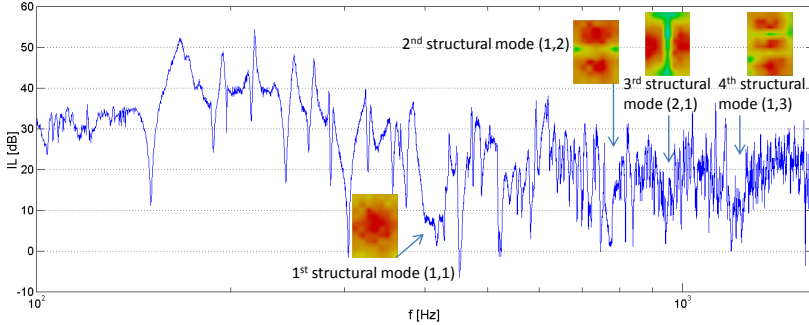


Figure 1.6: Experimental sound IL of the honeycomb sandwich panel. A2 size, clamped edges [1].

2.2.4 Numerical modal analysis in free edges conditions

A 2D multi-layered FE model of the honeycomb sandwich panel is built using MSC.Patran 2012. The size of the edges of each plate element of the model is 5 mm in order to have a convergence of the modal analysis results up to 3200 Hz. Two plies are used to represent the homogeneous Aluminium skins, while a layer with 2D orthotropic elastic properties is placed between them simulating the honeycomb core [8]. The numerical modal analyses are computed using MSC Nastran 2011.1, while the experimental-numerical correlation is evaluated using Virtual.Lab Rev11.

The experimental-numerical correlation between the first ten modes of the freely suspended modal analyses is reported in terms of the Modal Assurance Criterion (MAC) in

Table 1.2. The MAC provides a measure of consistency (degree of linearity) between estimates of a modal vector. It is a quality assurance indicator for experimental modal vectors that are estimated from measured frequency response functions. The high values of the same order modal pairs and the small frequency difference (on average less than 5%) indicate a good correlation between the experimental test and the numerical model. The same model is used to check the correlation of the clamped panel case.

Mode ID	Experimental Frequency[Hz]	Numerical Frequency[Hz]	MAC Value	Error (% of Experimental Frequency)
1	77.8	85.5	0.988	9.9
2	101.2	103.3	0.986	2.1
3	183.5	183	0.727	-0.3
4	185.5	198.6	0.935	7
5	228.9	237.6	0.974	3.8
6	284.8	297	0.906	4.3
7	365.2	372.8	0.981	2.1
8	373.7	390	0.978	4.4
9	465.2	473.4	0.984	1.8
10	509.4	528.3	0.974	3.8

Table 1.2: Experimental-numerical modes correlation table for freely suspended modal analyses - 600 * 800 mm² honeycomb sandwich panel [1].

Mode ID	Experimental Frequency[Hz]	Numerical Frequency[Hz]	MAC Value	Error (% of Experimental Frequency)
1	430.3	484	0.946	12.5
2	734.5	763.3	0.957	3.9
3	917	1000.5	0.941	9.1
4	1167	1187.4	0.871	1.7
5	1227.6	1228.1	0.945	0.04

Table 1.3: Experimental-numerical modes correlation table for clamped edges condition modal analyses A2 clamped honeycomb sandwich panel [1].

Similar to the free conditions case, the structural modal behaviour is well predicted by the multi-layered 2D model for the clamped conditions. Table 1.3 shows the good agreement

between numerical and experimental mode shapes and natural frequencies for the clamped configuration.

In order to numerically investigate the IL of the tested panel, a BE model of the cabin and the clamped honeycomb panel is used. Finite acoustic impedance is imposed at the inner walls of the cabin. The frequency independent real value of $140k \text{ kg/m}^2\text{s}$, corresponding to the acoustic impedance of typical polished concrete [9], is considered in order to take into account the finite (although small) sound absorption ability of these surfaces. Dissipative phenomena are also considered in the complex speed of sound, which represents the energy loss of the sound waves during their travel, more effective especially at higher frequencies. Structural damping is discarded.

Fig. 1.7 shows the comparison in narrow bands between experimental and numerical IL. A good prediction can be observed in the whole frequency range, from 150 Hz up to 1600 Hz, except in the band from 400 Hz up to 500 Hz. In this region, the first structural mode of the clamped panel occurs. The non-perfect clamped boundary conditions realized in practice have a big influence especially on the lower order modes. The first experimental mode occurs at 430 Hz, while numerically predicted at 480 Hz. Below 150 Hz the characteristics of the loudspeaker are too poor to provide a flat input spectrum. The discrepancy between 200 Hz and 250 Hz is due to the non-perfect clamping conditions of the real panel, whereas in the numerical model the panel is fully clamped. This in combination with a predominantly stiffness dominated panel response at these frequencies results in a mismatch of the predicted and measured IL.

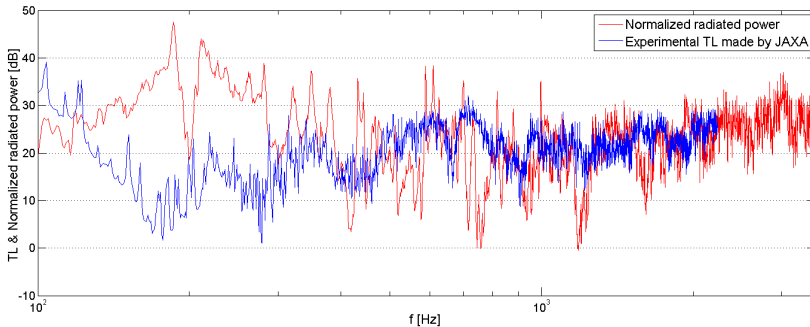


Figure 1.7: Experimental and numerical IL (narrow frequency) A2 clamped honeycomb sandwich panel [1].

2.2.5 Evaluation of the sound Transmission Loss

During the sound IL test, the Sound Pressure Level (SPL) inside the Soundbox can also be recorded by means of microphones placed inside the cavity. Their positions are chosen in order to avoid the influence of the interference phenomena close to the cavities walls (Fig. 1.8).

Considering the closed-cabin configuration, the difference between the internal averaged SPL and the externally radiated SPL is named here normalized radiated power. Fig. 1.9 shows the comparison between the experimental normalized acoustic power and the experimental TL, measured by Japanese Aerospace Agency (JAXA), of the same honeycomb sandwich panel but with a different size of $700 * 1000 \text{ mm}^2$.



Figure 1.8. Interior view of the Soundbox [1].

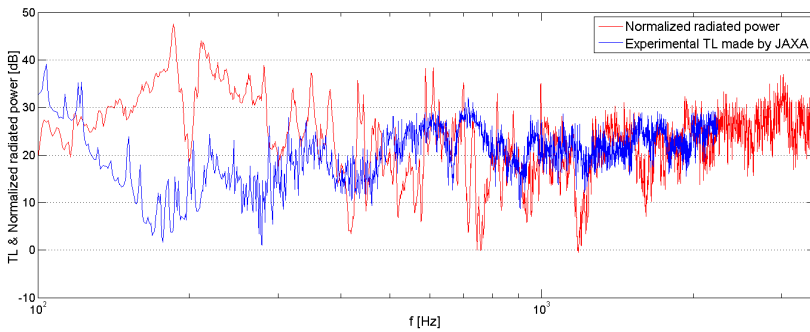


Figure 1.9: Normalized radiated power measured at KU Leuven A2 panel (red curve); Standard TL measured by Japanese Aerospace Agency (JAXA) 700*1000 mm panel (blue curve) [1].

The Soundbox reaches a diffuse field above 1600 Hz and, as shown in Fig. 1.9, here there is a good matching between the two curves, while below this frequency diffusivity is lost inside the Soundbox and the acoustic modal loading is becoming apparent, illustrating the value of the new test rig for vibro-acoustic characterization of panels with application in similar environments. Combining the above results with the correlations results from section 2.2.4 shows the high potential of the test rig to become a valuable tool for vibro-acoustic characterisation of lightweight panels under structural/acoustic loading and to determine standard TL values by means of non-standard measurements in a non-standard environment.

2.3 Conclusions

A new experimental setup to study the vibro-acoustic behavior of lightweight structures has been presented and discussed. Structural-acoustic coupled characteristic, coincidence frequency and acoustic IL can be measured in a fast and easy manner. The testing apparatus is designed to be small, movable, and consequently also able to provide repeatable measures and a desired and predictable low frequency acoustic field. The capability to have predictable acoustic characteristics of the presented facility, also in the fully modally dominated frequency region, become appealing for investigating noise and vibration properties of

lightweight components in a broadband frequency range. The aim is to extract useful parameters from the measured data, coming from a non-standard tool, in order to get a reliable prediction of the standard noise and vibration properties of lightweight panels themselves. Furthermore, the simplicity of the geometry does not require very sophisticated numerical models to provide satisfactory predictions of the measured behaviour in a very wide frequency domain. A wave based model can be easily prepared to this end to overcome the limitations of standard numerical techniques (FEM/BEM) at higher frequencies. This setup has been used to test a lightweight component, such as a honeycomb sandwich plate, in order to investigate its noise and vibration characteristics.

3 AN INVERSE APPROACH FOR THE ACOUSTIC MOBILITY CHARACTERIZATION OF A LIGHTWEIGHT PANEL TESTED IN A SMALL REVERBERANT CHAMBER

In the pervious chapter it has been analyzed the capability of having a prediction of the Insertion and Transmission Loss characteristic of small sized lightweight components by mean of a small reverberant chamber designed at KU Leuven (PMA Soundbox, left figure). To retrieve this acoustic property, the acoustic field inside the test rig has to be diffuse. For the PMA Soundbox, this condition is satisfied above 1600 Hz. As expected, it is possible to achieve a good prediction of the noise reduction properties above 1600Hz, while a discrepancy is evident in the low frequency range, where the field is not diffuse (Fig. 1.9. Here the modal vibro-acoustic coupling between the test rig and the tested panel affects too much the measurements .

Diffusivity problems are common for small reverberant chambers. in order to investigate this issue, analytical and numerical models have been employed to show the influence of different parameters in the sound reduction index at low frequencies [10, 11]. Teresa Bravo and Stephen J. Elliot [12] try to address the problem from an experimental point of view by proposing the use of an array of loudspeaker, driven by partially uncorrelated signal in the near field of the partition, in order to reproduce a diffuse sound pressure field impinging on the tested surface. Although there exist a lot of experimental and theoretical work on the variability of measurements at low frequencies, no effective solution has been found to address this problem. It still represents a big issue about obtaining a complete characterization of the noise reduction properties of lightweight structures and generating trustworthy numerical models to predict their behavior in practical applications.

Here a fast and new indirect procedure to retrieve the mobility matrix of structural components in the fully vibro-acoustic coupled frequency region is introduced, independently from the environment in which it is tested. The methodology allow for the determination of the panel's mobility by using the PTF (Patch Transfer Function approach) and involving (i)direct measurements of the Sound Pressure Level on the inner surface of a sample tested in a small cabin, (ii)good knowledge of the acoustic characteristics of the test rig. The aim is to develop a hybrid numerical-experimental procedure in order to get, from a not standard test rig such as a small reverberant cabin, a reliable prediction of the standard noise and vibration properties of lightweight panels.

This chapter is structured as follow: an overview of the PTF method and its applications is given in the first section, then the proposed methodology is explained in detail and validated with a numerical reference case. In the last section, conclusions and an overview on possible future works are listed.

3.1 The patch transfer function (PTF) approach

The PTF method has been initially developed with the goal to be a useful alternative tool to reduce the computational cost when solving coupled multi-system problems, while keeping a good accuracy in the results. Introduced by Ouisse et al. [13], it has been applied for acoustic coupling problems by Pavic [14], for a plate-cavity system by Aucejo et al. [15] and for transmission loss calculation of a multi-layer system by Chazot and Guyader [16]. A hybrid prediction scheme has been proposed and validate by Jan Rejlek et al. [17] to extend the PTF approach to vibro-acoustic systems containing numerically characterized fluid domains and experimentally characterized structural parts. Recently Veronesi et al. [18] implemented it to develop a novel experimental method for the characterization of poro-elastic materials.

3.2 The bases of the indirect approach

The PTF approach is modular, allowing for different procedures (numerical, experimental, analytical solution) to be used in order to assess impedance relation of each sub-system. The presented methodology takes advantage of this feature in order to develop an indirect procedure to characterize the mobility of a panel coupled to a small cabin excited by a set of acoustic sources. The first step is to divide the entire system in two subsystems coupled on an coupling surface, and then apply the the theorem formulated by Bobrovnskii [19]. If one of the sub-systems hosts sound sources while the other is passive, the global sound field can be represented by the superposition of two simpler field components: the field produced by the running sources with the coupling surface fully blocked (blocked pressure field), and the one due to the velocity, at the coupling surface of the coupled system, when the internal sources are switched off. Applying this principle at the panel inner surface, i.e. the coupling surface, it is possible to retrieve its mobility. What is required is the knowledge of the following three quantities: the global pressure field , the blocked pressure field and the surface impedance of the fully blocked coupling surface.

3.2.1 Governing equations

Let us consider a simple fully coupled vibro-acoustic system (Figure 1.10.a)consisting in a thin flat plate and a small cavity excited by a monopole source. For practical reasons the coupling surface is considered to match the interface of the two sub-system, i.e. the panel’s inner surface.

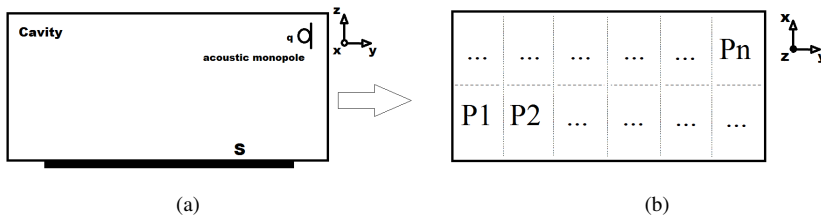


Figure 1.10: Vibro-acoustic system: cavity, vibrating surface and acoustic monopole (a) - Division of the vibrating surface in N patches (b). [2]

The PTF approach consists in subdividing the coupling surface S in N elementary surfaces ΔS_i (Figure 1.10.b), also referred to as patches. On each patch the dynamic quantities are

averaged and considered to assume a constant value. For the i -th patch, the averaged pressure and velocity are given by:

$$\bar{P}_i = \frac{1}{\Delta S_i} \int_{\Delta S_i} P_i(x, y) dS \quad (1.3)$$

$$\bar{V}_i = \frac{1}{\Delta S_i} \int_{\Delta S_i} V_i(x, y) dS \quad (1.4)$$

For the subsystem cavity, the transfer functions between the j -th excited patch and the i -th receiving one can be written in terms of blocked impedance as follow:

$$Z_{ij} = \frac{\bar{P}_i}{\bar{V}_j} |_{\bar{V}_{k \neq j} = 0} \quad (1.5)$$

For the subsystem plate the transfer functions between the j -th excited patch and the i -th receiving one can be written in terms of mobility as follow:

$$Y_{ij} = \frac{\bar{V}_i}{\bar{P}_j} |_{\bar{P}_{k \neq j} = 0} \quad (1.6)$$

Z_{ij} represents the averaged pressure \bar{P}_j of the i -th patch when a unit velocity is imposed on the j -th patch while keeping all the others patches blocked, i.e. $\bar{V}_k = 0$ for $k = 1, \dots, N$ and $k \neq j$.

Y_{ij} represents the averaged velocity \bar{V}_i of the i -th patch when a unit pressure is imposed on the j -th patch while keeping all the others patches free, i.e. $\bar{P}_k = 0$ for $k = 1, \dots, N$ and $k \neq j$.

Applying Eqs. 1.5 and 1.6 to all the patches, the impedance and mobility matrix \underline{Z} and \underline{Y} can be built. They are symmetric square matrix with dimensions $N*N$.

Considering the acoustic sub-domain (indicated by the superscript 1), the total pressure on the i -th patch of the coupling surface, can be expressed as:

$$P_1^i = P_b^i + Z_{blocked}^{ij} V_j \quad (1.7)$$

P_b^i is the averaged blocked pressure on the i -th patch due to the running source and keeping the coupling surface fully blocked.

V_j is the velocity, at the coupling surface of the coupled system, when the internal sources are switched off.

Writing Eq. 1.3 for each patch, the vectors \bar{P}_1 and \bar{V}_1 can be built. They are vectors of dimensions $N*1$ containing respectively the averaged pressures and velocities on every single patch. Eq. 1.3 can be than rewritten as follow:

$$\bar{P}_1 = \bar{P}_b + \bar{Z}_{blocked} \bar{V}_1 \quad (1.8)$$

Because of the continuity conditions between the two sub-systems, the pressures and velocities acting on the coupling surface have to be the same:

$$\bar{P}_1 = \bar{P}_2 = \bar{P}_{interface} \quad (1.9)$$

$$\bar{V}_1 = \bar{V}_2 = \bar{V}_{interface} \quad (1.10)$$

Considering that \bar{P}_2 and \bar{V}_2 are related by mean of the panel's mobility as follow:

$$\bar{V}_2 = \underline{Y}_{panel} \bar{P}_2 \quad (1.11)$$

Eq. 1.11 can be used together with the coupling conditions 1.9 and 1.10 in Eq. 1.8, and changing the sign of \bar{V}_2 when moving from sub-system 2 to subsystem 1, we obtain:

$$\bar{P}_S = \bar{P}_b - \underline{Z}_{blocked} \underline{Y}_{panel} \bar{P}_S \quad (1.12)$$

With some algebra Eq. 1.12 can be written as:

$$(\underline{I} + \underline{Z}_{blocked} \underline{Y}_{panel}) \bar{P}_S = \bar{P}_b \quad (1.13)$$

The aim is to indirectly retrieve the mobility matrix \underline{Y}_{panel} by using Eq. 1.13. For this purpose a matrix equation needs to be built. This goal can be reached by using a set of at least N acoustic loads. For the i -th acoustic excitation a vector equation like Eq. 1.13 can be written:

$$(\underline{I} + \underline{Z}_{blocked} \underline{Y}_{panel}) \bar{P}_S^i = \bar{P}_b^i \quad (1.14)$$

Writing Eq. 1.14 for each acoustic load, and considering that the matrices $\underline{Z}_{blocked}$ and $\underline{Y}_{surface}$ are constant, being characteristics of the system and independent from the acoustic load, a set of N equations can be built and grouped in a matrix form as follow:

$$(\underline{I} + \underline{Z}_{blocked} \underline{Y}_{panel}) \underline{P}_S = \underline{P}_b \quad (1.15)$$

where $\underline{P}_S = [\bar{P}_S^1 \quad \dots \quad \bar{P}_S^i \quad \dots \quad \bar{P}_S^N]$ and $\underline{P}_b = [\bar{P}_b^1 \quad \dots \quad \bar{P}_b^i \quad \dots \quad \bar{P}_b^N]$.
Eq. 1.15 can be solved for \underline{Y}_{panel} , obtaining:

$$\underline{Y}_{panel} = \underline{Z}_{blocked}^{-1} (\underline{P}_b \underline{P}_S^{-1} - \underline{I}) \quad (1.16)$$

Care has to be taken in the choice of the acoustic loads set. As shown in Eq. 1.16 the matrix \underline{P}_S has to be inverted, so the N acoustic excitations have to be such that a set of N independent pressure fields will be generated on the coupling surface.

The quantities \underline{Z}_{cavity} and \underline{P}_b are only related to the testing room and the complete knowledge of its properties (like for an in situ designed small reverberant chamber or for simple regular geometries) allows for calculating them via FEM/BEM or analytically. \underline{P}_S takes in account the global coupled response of the vibro-acoustic system and it can be experimentally achieved by mean of a set of microphones placed close by the inner surface of the tested panel.

3.3 A Numerical application of the methodology

The proposed approach is presented here by means of a numerical example and the acquired mobility matrix compared with a reference one. As a vibro-acoustic system, a small rectangular cavity coupled to an homogeneous aluminum plate is considered (Figure 1.10). The plate is 5 mm thick and its dimensions on the xy plane are 1.5 m and 0.3 m along x and y directions respectively. The panel surface is also considered as coupling surface, it covers entirely one wall of the cavity, which dimensions are then 1.5 m, 0.3 m and 0.4 m along x , y and z . Simply supported boundary conditions are imposed on each edge of the plate. The frequency range investigated goes from 0 Hz to 250 Hz.

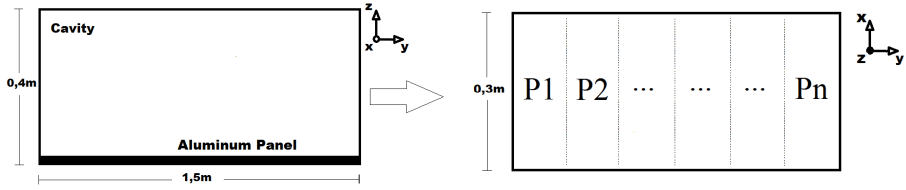


Figure 1.11. Rectangular cavity and Aluminum plate's size [2].

The material properties of the two subsystems are shown in Table 1.4.

Material	Density (Kg/m ³)	Phase speed (m/s)	Young's modulus (N/m)
Air	1,21	340	—
Aluminum	2770	—	72 * 10 ⁹
Material	Poisson's ratio (ν)	Damping ratio(ξ)	Absorption coefficient (α)
Air	—	—	0,005
Aluminum	0,33	0,001	—

Table 1.4: Material properties used for modeling the fluid inside the acoustic sub-domain and the Aluminum plate [2].

In order to choose an optimal configuration for the number of patches to be used and for the typology of the subdivision in patches for the structural sub-system, a modal analysis has been performed in advance. Table 1.5 shows acoustical and structural eigenfrequencies together with the associated number of half-wave along x and y , for the plate, and x , y and z for the cavity.

Subsystem	Order	Eigenfrequency [Hz]	Type
Cavity	1	0	(0,0,0)
	2	113	(1,0,0)
	3	227	(2,0,0)
Panel	1	141	(1,1)
	2	157	(2,1)
	3	184	(3,1)
	4	222	(4,1)

Table 1.5: The natural frequencies and semi-wave number of the related eigenmodes of each uncoupled system [2].

In the frequency range of interest the panel has only mode shapes having one semi-wave

along y , while the maximum number of semi-wave along x is four. The panel has been then divided in one row of 8 patches along x in order to have at least two patches for semi-waves in the whole frequency range analyzed. Is it important to underline that only one row of patches along y has been used because of the pressure will change predominantly along x resulting, in the analyzed frequency region, quite constant along y instead. Having another row of patches would translate in adding more load cases and creating bigger matrices, increasing the computational cost and decreasing the quality of the mobility matrix prediction. Indeed, at a fixed coordinate x , the pressure on the two patches along y would be almost the same, generating in the matrix \underline{P}_S linearly dependent rows which will give singularity problems.

3.3.1 The reference Mobility

The reference mobility matrix of the Aluminum plate has been calculated by mean of FEM analysis. A finite element model of the in vacuum plate with simply supported boundary conditions has been generated and 8 analysis have been performed. The i -th run consists in a frequency response analysis of the plate under a uniform unit pressure load acting on the i -th patch. At the i -th unit pressure load, the averaged velocity of the j -th patch corresponds to the component $Y_{reference}^{ij}$ of the reference mobility matrix, so, for each run, the structural frequency response has been averaged on each patch in terms of structural velocities allowing for the determination of the 8×8 $\underline{Y}_{panel}^{reference}$ matrix.

3.3.2 Blocked Impedance

The rectangular shape of the acoustic sub-system allows for the use of an analytical model, based on modal superposition, in order to determine the blocked impedance matrix $\underline{Z}_{blocked}$ on the coupling surface. In the acoustic sub-domain, the steady-state acoustic pressure perturbation field $p(r)$ is governed by the Helmholtz equation [20]:

$$\nabla^2 p(\mathbf{r}) + k^2 p(\mathbf{r}) = 0 \quad \forall \mathbf{r} \in \Omega_a \quad (1.17)$$

where k the acoustic wave number and c the speed of sound.

For a rectangular rigid cavity of dimensions Lx , Ly and Lz , the eigenmodes of the Helmholtz equation can be written as follow:

$$\phi_i(\mathbf{r}) = \zeta_i \cos\left(\frac{m_x(i)\pi x}{Lx}\right) \cos\left(\frac{m_y(i)\pi y}{Ly}\right) \cos\left(\frac{m_z(i)\pi z}{Lz}\right) \quad (1.18)$$

$$\zeta_i = \sqrt{2^s}, \quad s = \text{sign}(m_x(i)) + \text{sign}(m_y(i)) + \text{sign}(m_z(i)) \quad (1.19)$$

The Eigenfrequencies are:

$$\omega_i = \pi c \sqrt{\left(\frac{m_x(i)}{Lx}\right)^2 + \left(\frac{m_y(i)}{Ly}\right)^2 + \left(\frac{m_z(i)}{Lz}\right)^2} \quad m_x, m_y, m_z = 0, 1, 2, \dots \quad (1.20)$$

with the integers $m(i)$ chosen to give a monotonous increase of ω_i with i increasing, $i = 1, 2, \dots$. The patch-to-patch impedance between two patches of size Δx , Δy and $\Delta x'$, $\Delta y'$ centered at \mathbf{r} and \mathbf{r}' , respectively, is given by Pavic [14] as:

$$Z_{blocked}(\mathbf{r}, \mathbf{r}') = i\omega\rho c^2 \Delta x \Delta y \sum_i \frac{\phi_i(\mathbf{r})\phi_i(\mathbf{r}')}{\omega_i^2 - \omega^2 + 2i\varepsilon\omega} \operatorname{sinc}\left(\frac{m_{x,i}\Delta x}{2Lx}\right) \operatorname{sinc}\left(\frac{m_{y,i}\Delta y}{2Ly}\right) \operatorname{sinc}\left(\frac{m_{x,i}\Delta x'}{2Lx}\right) \operatorname{sinc}\left(\frac{m_{y,i}\Delta y'}{2Ly}\right) \quad (1.21)$$

where ε represents the equivalent damping due to a small wall absorption coefficient $\alpha \ll 1$, and it can be expressed as:

$$\varepsilon = \alpha c \frac{1}{Lx} + \frac{1}{Ly} + \frac{1}{2Lz} \quad (1.22)$$

The amplitude of a wave propagating with a speed c of is assumed to be reduced by α when traveling across the cavity length. Eq. 1.22 is based on the simplification that in the z direction the damping is only half of the values in the other directions. That is because along z one surface is used for the coupling, this surface is then blocked per definition and therefore rigid without any damping.

3.3.3 Results

In the last step, a set of $M > N$ different acoustic loads has been chosen and applied to (i) the FE model of the coupled vibro-acoustic system in order to retrieve \underline{P}_S , (ii) the FE model of the sole acoustic sub-system having the coupling surface blocked in order to retrieve \underline{P}_b .

The reason why the number of acoustic loads is bigger than the number of patches, i.e. the minimum number of loads to solve the set of equations, is related to the necessity to get N independent pressures vectors \underline{P}_S^i . How to obtain this goal is not known a priori, so $M > N$ load cases have been used with a random choice of the monopoles' positions and a pseudo-inverse matrix \underline{P}_S^{-1} has been calculated. A methodology to understand a priori how would be a set of exactly N load cases able to generate N independent pressure field \underline{P}_S^i is under investigation.

Using Eq. 1.16 the mobility matrix \underline{Y}_{panel} has been calculated and compared with the reference one $\underline{Y}_{panel}^{reference}$.

Is it possible to notice how the two curves matches really well in the frequency range of interest. A small shifting of the anti-resonant peaks can be observed; it is related to the averaging process of the velocity over the patches.

Figure 1.12 shows a comparison between the components (4,4) of the above mentioned matrices.

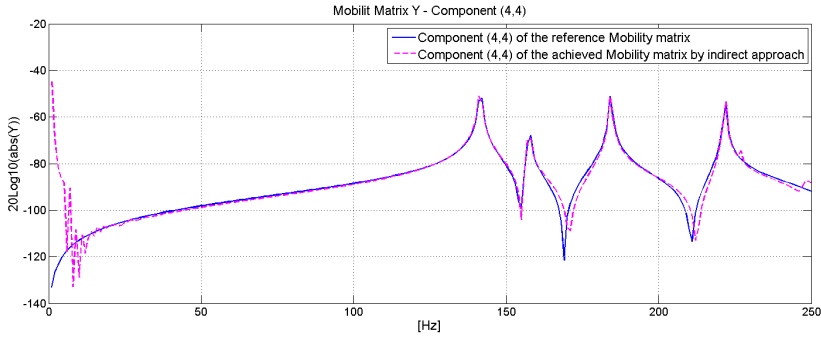


Figure 1.12: Comparison between the component (4,4) of the reference Mobility matrix (blue curve) and the achieved one by mean of an indirect approach (dashed magenta curve) [2].

3.4 Conclusions

The proposed procedure is an indirect approach that has shown the capability to accurately estimate the mobility matrix of a homogeneous Aluminum plate decoupled from the acoustic environment in which it is tested. The procedure has only been validated numerically, but the possibility to experimentally apply this method to a small reverberant chamber is quite appealing since (i) a coupled Sound Pressure Field can be achieved by acoustic measurements with a set of microphones placed inside the cavity, (ii) thanks to the deep knowledge about shape and acoustic properties of the test rig, it is possible to estimate the blocked impedance and blocked pressure matrices by means of numerical simulations involving FE method. Once the mobility matrix of the uncoupled panel is obtained, the transmitted sound under different standard sound pressure fields can be numerically evaluated. This will then allow for a standard-like noise reduction properties prediction.

The next step will be to develop an experimental procedure to completely validate the proposed approach on a real application case.

Moreover, other three possible scenarios about future research works are now possible:

- To investigate the capability of scaling the acquired Mobility and predict the noise reduction properties of a standard sample in a standard facility.
- To investigate the feasibility of performing sensitivity studies in order to: (i) understand the influence of the test rig to the acoustic properties of the tested sample, (ii) correct the measurements to achieve a trustworthy experimental prediction of the noise reduction properties, i.e. to achieve standard like results unaffected by the test environment.
- To extend the presented method to the study of noise reduction properties of multilayer systems.

About the last point listed above, it is worth to mention that, for studying noise reduction properties of multilayer structures, methodologies based on sub-structuring the global system are quite often used [16, 21, 22, 23]. Given a certain incident sound pressure field, the transmitted one is achieved going step by step through every single layer; so the knowledge of their characteristic impedance and/or mobility properties is crucial and not easy to get by a direct experimental procedure. A numerical approach is often used, so the possibility to experimentally apply the here introduced procedure is of great interest in order to tackle this issue in a faster, and easier to realize, way.

REFERENCES

- [1] V. D'Ortona, M. Vivolo, B. Pluymers, D. Vandepitte, and W. Desmet. Experimental identification of noise reduction properties of honeycomb panels using a small cabin. In *Proceedings of TRA 2014, the Transport Research Arena conference*, Paris, France, 2014.
- [2] V. D'Ortonai and E. Nijman. An inverse methodology for low-frequency transmission loss characterization of a lightweight panel in a small reverberant transmission suite. In *Proceedings of ICoEV 2015, the International Conference on Engineering and Vibration*, Ljubljana, Slovenia, 2015.
- [3] McKinsey&Company. Lightweight, heavy impact, 2012.
- [4] M. Vivolo. *Vibro-acoustic characterization of lightweight panels by using a small cabin*. PhD thesis, Katholieke Universiteit Leuven (KU Leuven), 2013.
- [5] M. Vivolo, B. Pluymers, D. Vandepitte, and W. Desmet. Vibro-acoustic study of lightweight components based on a new experimental setup. In *Proceedings of ICSV18 international congress on sound and vibration*, Rio de Janeiro, Brazil, 2011.
- [6] M. Vivolo, B. Pluymers, D. Vandepitte, and W. Desmet. An experimental-numerical study on the vibro-acoustic characterization of honeycomb lightweight panels. In *Proceedings of ISMA2010 conference*, Leuven, Belgium, 2010.
- [7] C. Gonzales Diaz, M. Vivolo, B. Pluymers, D. Vandepitte, and W. Desmet. Transmission suite design for vibro-acoustic characterization of lightweight panels. In *Proceedings of ISMA2010*, Leuven, Belgium, 2010.
- [8] Gibson and Ashby. *Cellular Solids: Structure and Properties. (2nd ed.)*. Cambridge University Press (CUP), 1999.
- [9] M. Norton and D. Karczub. *Fundamentals of noise and vibration analysis for engineers*. Cambridge University Press (CUP), 2003.
- [10] T. Kihlman. On the meaning of the sound reduction index at low frequencies. *Acustica*, 18:11–20, 1967.
- [11] W. Kropp, A. Pietrzyk, and T. Kihlman. Sound radiation into a rectangular room. applications to airborne sound transmission in buildings. *Acta Acustica*, 2:379–392, 1994.
- [12] T. Bravo and S. J. Elliott. A simulation analysis of low frequency sound transmission measurements. In *Proceedings of International Congress on Acoustic 2004*.
- [13] M. Ouisse, L. Maxit, C. Cacciolati, and J. Guyader. Patch transfer functions as a tool to couple linear acoustic problems. *Journal of Vibration and Acoustics*, 127:458–466, 2005.
- [14] G. Pavic. Air-borne sound source characterization by patch impedance coupling approach. *Journal of Sound and Vibration*, 329(23):4907–4921, 2010.
- [15] M. Aucejo, L. Maxit, N. Totaro, and J. Guyader. Convergence acceleration using the residual shape technique when solving structure-acoustic coupling with the patch transfer functions method. *Computers & Structures*, 88(11-12):728736, 2010.

- [16] J. Chazot and J. Guyader. Prediction of transmission loss of double panels with a patch-mobility method. *Journal of the Acoustical Society of American*, 121:267–278, 2007.
- [17] J. Rejlek, G. Veronesi, C. Albert, and E. Nijman. A combined computational-experimental approach for modelling of coupled vibro-acoustic problems. In *Proceedings of Society of Automotive Engineers 2013 Noise and Vibration Conference and Exhibition*, Grand Rapids, Michigan, USA, 2013.
- [18] G. Veronesi, C. Albert, E. Nijman, and J. Rejlek. Patch transfer function approach for analysis of coupled vibro-acoustic problems involving porous materials. In *Proceedings of Society of Automotive Engineers 2014 Noise and Vibration Conference and Exhibition*, Graz, Austria, 2014.
- [19] Y. I. Bobrovnskii. A theorem on the representation of the field of forced vibrations of a composite elastic system. *Acoustical Physics*, 47:507–510, 2001.
- [20] F. Fahy. Sound and structural vibration: Radiation, transmission and response. *Journal of Sound and Vibration*, 233(4):699–705, 2000.
- [21] M. Villot and al. Predicting the acoustical radiation of finite size multi-layered structures by applying spatial windowing on infinite structures. *Journal of sound and vibration*, 245(3):433–455, 2001.
- [22] M. Villot and al. Using spatial windowing to take the finite size of plane structure into account in sound transmission. In *Proceedings of International Conference on Emerging Technologies of Noise and Vibration Analysis and Control 2005*, Saint Raphael, France, 2005.
- [23] H. Nelisse and T. Onsay and N. Atalla. Structure borne insertion loss of sound package components. In *Proceedings of Society of Automotive Engineers 2003 Noise & Vibration Conference and Exhibition Technical Papers*, Traverse City (MI), 2003.

Chapter 2

Cylindrical Nearfield Acoustical Holography

MATTEO KIRCHNER^{1,2,3}, *EUGÈNE NIJMAN*²

¹ *KU LEUVEN, DEPARTMENT OF MECHANICAL ENGINEERING*

² *VIRTUAL VEHICLE RESEARCH CENTER*

³ *MEMBER OF FLANDERS MAKE*

1 EXECUTIVE SUMMARY

Automotive industry is asking for new methodologies to characterise the acoustic emissions of electric motors, since their integration in electric vehicles and plug-in-hybrid vehicles is growing.

This chapter presents some research developments of Nearfield Acoustical Holography (NAH) in cylindrical coordinates. In fact, this experimental technique is well suited for the characterisation of acoustic sources such as electric motors.

The theory behind cylindrical NAH is briefly outlined here. A possible limitation of NAH is the need of an overwhelming amount of microphones in the high frequency range, governed by the Nyquist-Shannon sampling theorem. A possible approach to reduce the number of sensors is the so-called compressive sensing. Its formulation, theoretical background and applicability are discussed.

Two numerical test cases are developed to support the theory. First, practical aspects of the classical NAH such as microphone positioning error, measurement noise, hologram distance and measurement aperture are investigated and discussed. Moreover, a second test case helps to understand the applicability of compressive sensing to NAH.

2 INTRODUCTION AND GENERAL FRAMEWORK

Automotive industry is increasingly driven by the need to offer fuel efficient and eco-friendly mobility. In fact, legislators are reducing carbon dioxide limits in order to reach the targets set by international agreements. At the same time, customers are asking for comfortable and innovative vehicles.

The reduction of fuel consumption and pollution is mainly achievable by lightweight

design, downsizing internal combustion engines (ICEs), and through electrification and hybridisation of the vehicle's powertrain.

Unfortunately, these new measures motivated by the pressure to lower both the exhaust emission levels and the fuel consumption present new design challenges in the vehicle design process. For example, downsizing conventional ICEs leading to higher vibration levels due to the reduced number of cylinders.

Moreover, under some powering strategies (such as parallel hybrid) multiple propulsion systems are asked to operate automatically according to the driving conditions, with important NVH issues linked to the switch from one configuration to another. For other typologies, an ICE works as range extender, generating a constant noise and vibration level that does not depend on the driving speed, which may be annoying for the driver and the other vehicle occupants.

Pure electric driving is known to produce a low overall noise level, but a tonal component generated by the electric motor(s) may dominate the sound emission and be annoying. Furthermore, secondary noise components such as wind, tire-road friction and powertrain become audible.

Finally, the global noise reduction raises the well-known security issues regarding low-speed traffic such as pedestrians and cyclists.

In this framework, it is clear that automotive industry is asking for new methodologies to characterise the acoustic emissions of electric components. This chapter focuses on an experimental methodology to characterise the noise emissions of an electric motor, based on Nearfield Acoustical Holography (NAH) in cylindrical coordinates. This technique allows the evaluation of sound intensity, as well as pressure level and particle velocity. It is suitable for any type of electric motor without knowing either the internal geometry or the material properties.

This chapter is divided in two parts. The first part (sections 3–4) is theoretical, with section 3 discussing the classical NAH approach in cylindrical coordinates, together with a regularisation procedure to limit the influence of noise. Next, section 4 introduces compressive sensing as a possible way to limit the number of measurements which are required by the classical NAH in the high frequency range. The feasibility of this approach is also taken under consideration.

The second part of this chapter (sections 5–6) presents a few numerical experiments. Section 5 focuses on simulations to understand some practical aspects to be taken into account while performing NAH in cylindrical coordinates. Section 6 shows and discusses a simple test case in which compressive sensing is applied to NAH. Finally, section 7 summarizes the conclusions.

3 CYLINDRICAL NAH

Nearfield Acoustical Holography (NAH) is an experimental technique that allows an accurate characterisation of a source through the inverse propagation of a hologram. NAH is described exhaustively in a book by Earl G. Williams [1], where formulas are given for planar, cylindrical and spherical geometries.

NAH in cylindrical coordinates is extremely well suited for cylindrical sources like electric motors. This section follows the research stream first proposed in [2] and subsequently documented in [3]. First, subsection 3.1 outlines the classical cylindrical NAH, while section 5 will show a numerical test case, which presents a different geometry as well as different parameters if compared to references [2, 3].

3.1 Problem formulation and solution regularisation

Cylindrical Nearfield Acoustical Holography consists in four steps. First, pressure measurements (or alternatively particle velocity measurements [4, 5]) are acquired on a grid of points on a cylindrical surface (the hologram lattice). The second step involves the computation of the angular spectrum through a spatial transform, which gives a wavenumber space (k-space) description of the original distribution. Furthermore, this angular spectrum is multiplied by an inverse propagator for the reconstruction of the pressure or velocity distribution on the target surface. If the target surface corresponds to the source surface, the source velocity distribution may be obtained. Finally, the results are transformed back to the real space.

The NAH procedure may be rewritten as an inverse problem, which is likely to be mathematical ill-posed. The reason why NAH is prone to instability can be found in the distinction between evanescent and non-evanescent waves, and their way of propagating in a medium. Evanescent waves decay exponentially or follow power law decay, depending on the geometry (planar, cylindrical, spherical). Those behaviours lead to an ill-posed inverse problem, where they turn into exponential-like amplifications causing the blowing up of the measurement noise. Several regularisation methods are available to deal with such problem [6, 7, 8, 9], and Tikhonov regularisation has been chosen here.

NAH can be formulated as a single matrix expression. First, let us consider the forward problem shown in eqs. (2.1–2.2) [9], where p is the spatial pressure distribution at a given frequency and w is the velocity distribution on the source. Matrix H is built from a diagonal matrix G containing the direct propagators of each k-space component, pre-multiplied by an inverse DFT matrix F^{-1} , and post-multiplied by F .

$$p = Hw \quad (2.1)$$

$$H = F^{-1}GF \quad (2.2)$$

The inverse problem is shown in eqs. (2.3–2.4), where R_β is the Tikhonov regularised inverse, which depends on the regularisation parameter β . Superscript H denotes the Hermitian matrix (*i.e.*, the conjugate transpose). Note that if $\beta = 0$ (no regularisation), R_β is simply the pseudo-inverse of H .

$$w = R_\beta p \quad (2.3)$$

$$R_\alpha = (H^H H + \beta I)^{-1} H^H \quad (2.4)$$

For increasing β , Tikhonov regularisation progressively reduces the impact of the singular values, starting from the smallest ones. For this reason, it behaves as a low-pass filtering in k-space.

Among the several methods to seek the value of β that best regularises R_β [6, 9], the generalized cross validation (GCV) offers a way to get to a very accurate solution without the need to know the variance of the noise of the system [9].

The GCV imposes to minimize a functional [8], and it is referred to as “the leaving-one-out method”, *i.e.*, one measurement point at a time is omitted from the NAH procedure and used as a reference. The optimal β yields the best reconstruction in the omitted points in a least mean square sense [8].

The straightforward implementation of the functional suggested in [8] leads to a very high computational effort. A much more time-efficient algorithm is described in [9].

It is important to emphasize that the GCV scheme is not able to stabilize the problem if the noise components are highly correlated [6].

It is worth to notice that the k -space components are obtained by a two-dimensional discrete Fourier transform (2D-DFT). The sensor spacing is thus governed by the Nyquist-Shannon sampling theorem, leading to an overwhelming amount of transducers in the high frequency range, limiting the practical application of NAH.

4 NAH WITH COMPRESSIVE SENSING

Promising results have been published with regard to compressive sensing (CS) applied to NAH with the aim to reduce the number of microphones without affecting the quality of the reconstruction [10]. Compressive sensing is a well known scheme in the field of audio and image processing, and it allows to slim down data at the source. CS wants to directly acquire the minimum amount of data which is needed to fully represent a signal. In some fields such as digital photography a huge amount of data is acquired and immediately compressed in order to fit in a storage drive.

Compressive sensing is based on a concept referred to as signal sparsity, *i.e.*, a signal can be represented (fully or in an approximate way) by just a few components belonging to a certain transformed space. This space is referred to as dictionary, and its components are the so-called basis functions.

Signals are compressible, *i.e.*, they are well approximated by sparse representations, when they have a sparse representation in some domain [11, 12, 13]. The problem is then to represent a signal in that specific domain and keep only the relevant non-zero elements (the sparsest the solution, the better the compression). A simple overview on compressive sensing can be found in [13].

Most of the material regarding the application of compressive sensing to NAH comes from reference [14], and the reader can refer to it for further details. A brief overview can be found also in [3], without any numerical example.

4.1 Problem formulation

According to the notation that has already been introduced while describing the classical NAH procedure in section 3, this subsection deals with the formulation of holography with compressive sensing, highlighting its structure and complexity in comparison to eq. (2.1).

Formally, the only difference is in the definition of the source velocity distribution w , which is shown in eq. (2.5).

$$w = D\alpha \tag{2.5}$$

Matrix D is a dictionary of basis functions and α is a complex column vector containing the coefficients of those basis functions. Dictionaries may be overcomplete [15], meaning that the signal description expressed by eq. (2.5) is not unique, *i.e.*, one basis function can be represented by other basis functions. Mathematically, this corresponds to a non-orthogonal dictionary. Such characteristic can result from either the fact that a dictionary has been designed that way, or because some orthogonal dictionaries (complete dictionaries) are merged together [15].

There are many existing candidates for the composition of a dictionary for compressing sensing, such as Fourier basis functions, wavelets, chirplets [10]. The crucial point is that the

dictionary has to be able to *sparsify* the signal, *i.e.*, only a few atoms should (fully or in an approximate way) describe the signal.

A first step towards the formulation of NAH with compressive sensing can be obtained by substituting eqs. (2.2) and (2.5) in (2.1), resulting in eq. (2.6). It will become clear later that matrix F^{-1} cannot be obtained by matrix inversion. For this reason, eq. (2.6) is rewritten as shown by eq. (2.7), which is discussed in the upcoming list.

$$p = F^{-1}GFD\alpha \quad (2.6)$$

$$p = F_{inv}GFD\alpha \quad (2.7)$$

- $p \in \mathbb{R}^{m \times 1}$ contains the measurements, sampled in space. It consists of complex numbers, since each measurement point carries the frequency domain information at a frequency step. The measurement points may or may not be regularly spaced. A randomly spaced hologram helps to capture the high frequency information with fewer measurements in comparison to the number imposed by the Nyquist-Shannon sampling theorem [10].
- $\alpha \in \mathbb{R}^{n \times 1}$ carries the complex coefficients of the basis functions. It should be as sparse as possible, in order to allow fewer measurement points in comparison with classical holography [12, 11].
- $D \in \mathbb{R}^{l \times n}$ is the dictionary. Its columns are the n basis functions (atoms). Each basis function is evaluated on a set of l regularly spaced points. The choice of l determines the number of spatial Fourier components that will be propagated through G . The finer the sampling, the higher the number of (evanescent) components taken into account.
- $F \in \mathbb{R}^{l \times l}$ is a square matrix that applies the two-dimensional discrete Fourier transform (2D-DFT) to the basis functions.
- $G \in \mathbb{R}^{l \times l}$ has the same size of F . It is a diagonal matrix containing the (complex) propagators related to the corresponding Fourier components. The propagators are defined here for the forward problem (exterior problem), *i.e.*, the propagation goes from the source to the (cylindrical) surface on which the hologram is located.
- $F_{inv} \in \mathbb{R}^{m \times l}$ can not be computed by inverting F , as it was in eqs. (2.2) and (2.6). This is because it may not be square (typically, $m < l$). Moreover, it may be evaluated on a set of randomly spaced points, accordingly to the m measurement positions.

Eq. (2.7) can be written in the compact version shown by eq. (2.8), where A is the so-called global sensing matrix, defined in eq. (2.9). This formulation highlights the measurements vector p , the (sparse) complex coefficients vector α , and matrix A between them.

$$p = A\alpha \quad (2.8)$$

$$A = F_{inv}GFD \quad (2.9)$$

Since the general aim of compressive sensing is to reduce the number of measurement points, there will always be more basis functions than measurement points, *i.e.*, $n > m$.

Consequently, the system described by eqs. (2.8–2.9) is underdetermined, *i.e.*, there are fewer equations (measurement points) than unknowns (basis functions).

In order to reconstruct the signal, eq. (2.8) has to be inverted and computed. The solution has then to be insert into eq. (2.5) to obtain the velocity distribution.

Among the infinite number of solutions that an underdetermined system such as eq. (2.8) has, the sparsest solution is the best candidate for the success of compressive sensing. The common Moore-Penrose pseudo-inverse (which relies on a ℓ_2 norm optimisation, *i.e.*, on the least mean square error) does not address this specification [11].

Given an arbitrary underdetermined system such as eq. (2.8), the sparsest among all possible solutions is obtained by a minimization of the ℓ_0 norm of the vector α [16], as shown in eq. (2.10).

$$\min_{\alpha} \|\alpha\|_{\ell_0} \text{ subject to } A\alpha = p \quad (2.10)$$

Unfortunately, there are no efficient algorithms to solve such problem, due to the non-convexity of the ℓ_0 norm optimisation [17, 16]. Fortunately, those limitations can be overcome by “relaxing” the ℓ_0 norm up to an ℓ_1 norm problem [18, 19], for the solution of which some methods are available [15].

The so-called basis pursuit (BP) has recently been strongly developed. BP is capable to find the sparsest solution within an overcomplete (non-orthogonal) dictionary [15, 20], while other methods need the basis functions to be orthogonal. Moreover, BP is based on global optimisation, offers better sparsity and stable superresolution, and can be used with noisy data [15].

Under some conditions, which will be discussed in section 4.2, both the ℓ_0 and ℓ_1 problems are proven to give the same and unique result. The relaxation from ℓ_0 norm to ℓ_1 norm of eq. (2.10) leads to the new problem described by eq. (2.11), the solution of which will be sought through a basis pursuit algorithm [15].

$$\min_{\alpha} \|\alpha\|_{\ell_1} \text{ subject to } A\alpha = p \quad (2.11)$$

In case of solution approximation, regularisation and noise filtering, a slightly different approach is known as basis pursuit denoising (BPDN) [15].

In the next section, the applicability of the methodology that has been presented up to here will be discussed.

4.2 Feasibility

Since the publication of the first milestones regarding compressive sensing by Donoho [18] and by Candès, Romberg and Tao [21, 17], a huge amount of literature can be found. Some papers are written by the same authors and include a few extensions of the already mentioned references (*e.g.*, [12, 22]), while other researchers applied the theory to image compression, which seems to be the most interested field of application.

In order to get the correct results of eq. (2.10) through the solution of eq. (2.11), having few measurement points and few non-zero basis functions, the matrices of the undetermined system have to satisfy a condition known as restricted isometry property (RIP) [16]. The RIP characterises matrices which are nearly orthonormal, at least when operating on sparse vectors.

After defining the RIP (subsection 4.2.1), it will be explained in subsection 4.2.2 that unfortunately it cannot be satisfied when performing NAH.

4.2.1 The restricted isometry property (RIP)

Let us consider the linear system described by eq. (2.8) and the ℓ_1 problem described by eq. (2.11). The restricted isometry property is a matrix condition which is set by means of some *restricted isometry constants*, defined as the smallest number δ_S such that eq.(2.12) holds for all S -sparse vectors ($S \leq K$, so that δ_S is defined for every $S = 1, 2, \dots, K$) [22]. A vector is said to be S -sparse if it has at most S nonzero entries.

$$1 - \delta_S \leq \frac{\|A\alpha\|_{\ell_2}^2}{\|\alpha\|_{\ell_2}^2} \leq 1 + \delta_S \quad (2.12)$$

Saying that a matrix A satisfies a certain RIP means that for any arbitrary vector α having $S \leq K$ nonzero entries, the result of eq. (2.12) stays confined in a certain band. In other words, there is a certain sparsity K below which the amplification introduced by the matrix transformation remains bounded.

Starting from this definition of RIP, reference [22] states that:

- if $\delta_{2S} < 1$, the ℓ_0 problem of eq. (2.10) has a unique S -sparse solution, *i.e.*, if one can prove that for a certain level of sparsity S any vector α with sparsity up to $2S$ will amplify the matrix $[A]$ less than a factor of 1 (when normalized by $\|\alpha\|_{\ell_2}^2$), there is a unique solution with sparsity S .
- if $\delta_{2S} < \sqrt{2} - 1$, the solution to the ℓ_1 problem of eq. (2.11) is that of the ℓ_0 problem of eq. (2.10), and the convex relaxation is exact, *i.e.*, if one can prove that for a certain sparsity S any vector α with sparsity up to $2S$ will amplify the matrix $[A]$ less than a factor of $\sqrt{2} - 1$ (when normalized by $\|\alpha\|_{\ell_2}^2$), then the solution of the ℓ_1 problem corresponds to the sparsest solution that the ℓ_0 problem would give.

The condition $\delta_{2S} < \sqrt{2} - 1$ corresponds to having the RIP satisfied (*i.e.*, the RIP condition holds) [12].

The definition of RIP paved the way to further studies about the required number of measurements and possible way to enhance the RIP. Reference [12] proposes a formula for the required number of measurements, depending on the sparsity level. If this formula is satisfied and if the global sensing matrix A is a Gaussian random matrix, then it is highly possible that the RIP is satisfied. This implies an *a priori* knowledge of the signal, which may be problematic for the characterisation of an unknown source.

It is then extremely important to find a dictionary which sufficiently sparsifies the signal. It must be underlined that this might not be trivial, especially for NAH applications, since the velocity field may be unknown.

Some attempts to improve the RIP involve dictionary learning [23, 24, 25] and the so-called measurement matrix (also referred to as sensing matrix) [11, 26]. In order to go beyond the Nyquist-Shannon limit, measurement have to carry the high frequency information. This can be achieved substituting the classical regular sampling with a random sampling (in space for images, in time for time-signals) [10].

Please note that both a random measurement matrix and a low matrix coherence are not sufficient conditions to have the RIP satisfied, *i.e.*, they are just tools to enhance (but not guarantee) the RIP.

4.2.2 RIP with Holography

In this paragraph, it will be shown that for acoustical holography it is not possible to satisfy the RIP. The main reason for this has to be found in the matrix G containing the propagators, already introduced in eq. (2.2). Before dealing with this crucial issue, a simplified problem is introduced.

Eq. (2.7) can be rewritten in a simplified version if D is a Fourier dictionary, such that eq. (2.13) applies. Dimensions n and l are the same, *i.e.*, the number of basis functions is equal to the number of the Fourier components.

$$FD = I \quad (2.13)$$

The original signal must contain only a few Fourier components, so that α can be sparse. Accordingly, eqs. (2.7–2.9) become as shown in eqs. (2.14–2.16). Σ replaces then A for the simplified situation set by eq. (2.13).

$$p = F_{inv}G\alpha \quad (2.14)$$

$$p = \Sigma\alpha \quad (2.15)$$

$$\Sigma = F_{inv}G \quad (2.16)$$

Let us first focus on G , which is a square diagonal matrix containing the velocity propagators (g_v) of each wavenumber component. Their formula is presented in eq. (2.17) for a cylindrical geometry [1], where j is the complex variable, Z_0 is the acoustic impedance of the medium (*e.g.*, air), k_0 is the wavenumber of the medium at a given frequency, H_n is the Hankel function of the n^{th} circumferential order, H_n^I is the first derivative of H_n , k_r is defined through k_0 and the longitudinal wavenumber (k_z) as follows: $k_r = \sqrt{k_0^2 - k_z^2}$, r_h is the radius of the cylindrical measurement surface (hologram), and finally a is the radius of the cylindrical source. The hologram distance is then $d = r_h - a$.

$$g_v = \frac{jZ_0k_0H_n(k_r r_h)}{k_r H_n^I(k_r a)} \quad (2.17)$$

Fig. 2.1 shows the propagators as a function of the circumferential order, *i.e.*, the circumferential wavenumber (k_θ) multiplied by the source radius a . The propagators have been evaluated for a simple one-dimensional case corresponding to an infinite cylinder ($k_z = 0$ such that $k_r = k_0$), for hologram distances from $d = 0$ m to $d = 0.2$ m and step 0.05 m. The graph refers to a source with radius $a = 0.1$ m radiating in air at a frequency $f = 5000$ Hz.

It can be seen that as d assumes higher values, a different amplification is given to propagating and evanescent components (low and high circumferential orders, respectively).

Having clarified the structure of G , it should now be easy to understand that a good RIP cannot be obtained, not even pre-multiplying it by a random matrix. The difference in the amplification of the k -space components precludes the restricted isometry constants to stay within the RIP limits (*i.e.*, $\delta_{2S} < \sqrt{2} - 1$).

Let us now move on to F_{inv} , which represents an inverse two-dimensional Fourier transform evaluated at the measurement points. Its elements $f_{inv}(k, n)$ assume the formula shown in eq. (2.18), where k and n refer to the measurement position and the Fourier component, respectively.

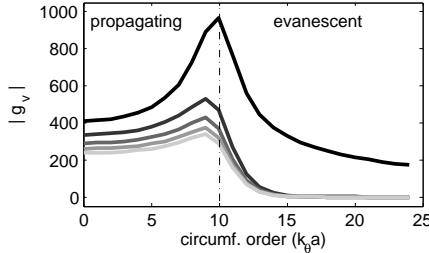


Figure 2.1: $|g_v|$ in air for $f = 5000$ Hz and $a = 0.1$ m. The colour shade gets lighter while d increases from 0 to 0.2 m, and step 0.05 m.

$$f_{inv}(k, n) = e^{+j2\pi kn} \quad (2.18)$$

The real and imaginary part of $f_{inv}(k, n)$ oscillate according to k and n , but its absolute value is constant for every combination (k, n) . In such scenario, a random microphone positioning cannot create a Gaussian random matrix A (or Σ), which would most likely satisfy the RIP.

Thus, for NAH applications it is not possible to increase the rate of success of the basis pursuit algorithm just by randomizing the microphone positions, because of the structure of the matrices. This randomization is only needed to include information about higher frequency components, which cannot be captured by a regular lattice due to the Nyquist-Shannon limit.

5 CYLINDRICAL NAH: NUMERICAL EXPERIMENTS

This section presents a set of numerical experiments to investigate practical aspects of cylindrical holography such as microphone positioning error, background noise and measurement aperture. This section follows the procedure proposed in [2], adapting it for a different geometry as well as different settings.

5.1 Test case

The test case presented in this subsection involves a cylindrical source of length $l = 0.24$ m and radius $a = 0.1$ m, being a representative size for automotive applications such as electric traction motors for green mobility.

A set of acoustical monopoles which are positioned on a cylindrical grid inside a virtual source surface (Fig. 2.2), consisting of a superellipsoid with smooth, almost cylindrical shape. The volume velocity distribution of the monopoles was chosen in order to obtain the frequency independent source surface velocity distribution presented in Fig. 2.3. In order to do so the source simulation technique (SST) [27] was used. The sound pressure in any position of the radiated field can be obtained by straightforward superposition of the monopole fields.

Fig. 2.4 shows the hologram lattice, on which the sound pressures are measured. Unless otherwise stated, the length of the hologram is set to 1.5 times the length of the source, and the distance from the hologram to the surface of the source is $d = 0.04$ m. Moreover, the spatial

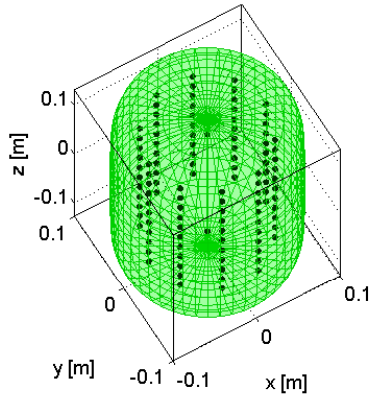


Figure 2.2: Source layout. Virtual source geometry (green surface) and acoustic monopoles for the source simulation technique (black dots).

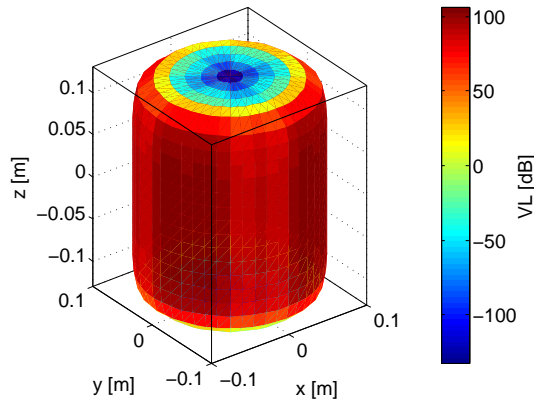


Figure 2.3: Frequency independent target normal velocity level (VL) for the source simulation technique (SST).

sampling is chosen in such a way that the unwrapped mesh presents a similar microphone spacing in the two directions (longitudinal and circumferential sampling $\Delta \approx 0.05$ m). Under these spatial sampling conditions, the frequency limit set by the Shannon sampling theorem is $f = \frac{c_0}{2\Delta} \approx 3430$ Hz (in air, where the speed of sound is $c_0 \approx 343$ m/s).

A finer lattice can be designed if higher frequencies have to be taken into account. However, increasing the amount of microphones may modify the sound field around the source (because of the wave-microphone interaction). Moreover, the data acquisition system may become much more expensive due to the higher number of channels required.

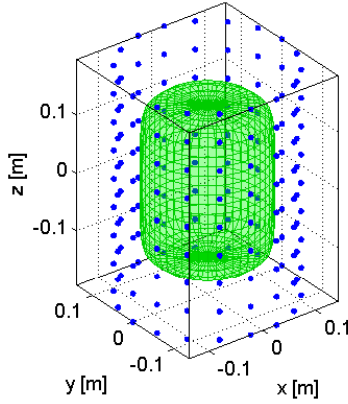


Figure 2.4. Source geometry (green surface) and hologram (blue dots).

5.2 Effects of the regularisation

To show the effects of the regularisation, a small error of zero mean and standard deviation $\sigma = 0.25$ dB was added to the simulations. Fig. 2.5 shows the effect of the regularisation procedure on the surface velocity reconstruction along the z axis at $\theta = 0.35$ rad and along the circumference at $z = 0$ m. The graphs include the reference velocity distribution generated by the acoustic monopoles (solid gray), and the NAH result with and without regularisation (dashed green and dotted blue, respectively). The velocity level is expressed in dB as $VL = 10 \cdot \log_{10}(\frac{v^2}{v_{ref}^2})$, with $v_{ref} = 5 \cdot 10^{-8}$ m/s.

The results obtained without regularisation are far from being accurate, while the situation completely changes with the regularisation. In particular, a good reconstruction of the velocity distribution is observed in the region of the source (between the vertical dotted black lines in Fig. 2.5).

Fig. 2.6 shows the spatial averaged square error (ε) of the hologram portion corresponding to the source, for a frequency range from 10 to 3410 Hz, and step 100 Hz. Variable ε is defined in eq. (2.19), where v_0 represents the actual source velocity. The bar indicates spatial average.

$$\varepsilon = 10 \cdot \log_{10} \left(\frac{\overline{v^2}}{v_0^2} \right) \quad (2.19)$$

At high frequencies the k -space components exceed the noise and regularisation is not necessary, while at low frequencies the low-pass k -space filter introduced by the regularisation is absolutely necessary and gives excellent results.

5.3 Simulations

5.3.1 Hologram length

For cylindrical NAH, an ideal example that lacks any noise cannot be considered due to the spectral leakage in the longitudinal direction, along which the system is not periodic.

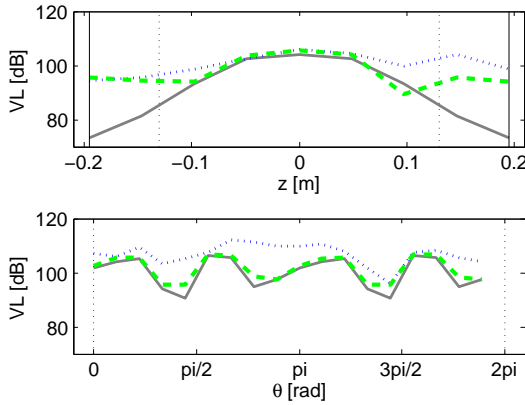


Figure 2.5: Effect of the regularisation procedure on the surface velocity reconstruction along the z axis at $\theta = 0.35$ rad (top) and along the circumference at $z = 0$ m (bottom). Legend: real velocity distribution (solid gray), NAH not regularised (dotted blue), NAH regularised with Tikhonov and GCV (thick dashed green). The graphs refer to $f = 1200$ Hz. The vertical black lines in the top figure help to visualize the geometry: the dotted line represent the limit of the source, while the solid lines are the longitudinal limits of the hologram.

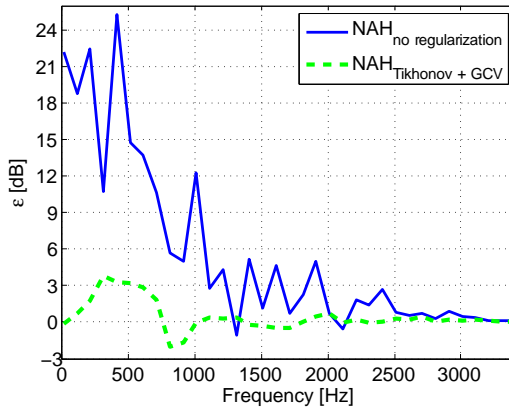


Figure 2.6: ϵ from 10 to 3410 Hz and step 100 Hz. $d = 0.04$ m and $\Delta \approx 0.05$ m. NAH not regularised (dashed green), and NAH regularised with Tikhonov and GCV (solid blue).

To limit the influence of this phenomenon, the hologram has to be sufficiently long and sufficiently close to the surface of the source, to keep the replicated sources far from the real source. It is consequently important that the microphones which are located nearby the two ends of the hologram measure a much lower pressure than the ones in the central part. On top of this, the hologram distance has to be set as small as possible also in order to detect the exponentially decaying evanescent waves. A distance of 0.04 m has been chosen here.

Fig. 2.7 shows the influence of the hologram length, for a fixed hologram distance and spatial sampling. With the exception of the shortest length, all other curves oscillate within

3 dB at low frequency, and become very small above 1500 Hz. Since the results with a hologram of 1.5 times the length of the source are judged accurate enough, this length has been chosen as reference for the simulations, limiting the number of microphones.

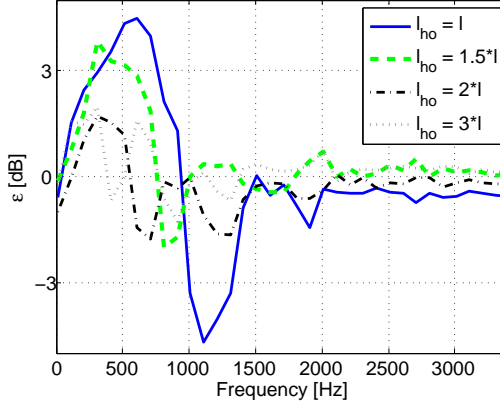


Figure 2.7: ε for four different hologram lengths, from 10 to 3410 Hz and step 100 Hz. $d = 0.04$ m and $\Delta \approx 0.05$ m. l_{ho} and l are the lengths of the hologram and the source, respectively.

5.3.2 Hologram positioning error

A certain level of accuracy characterises the position of the sensors. Stochastic and systematic positioning errors are distinguished and discussed here.

Stochastic errors are due to the accuracy that can be achieved while aligning the acoustic center of the pressure transducers with their theoretical positions on the holographic lattice. This type of error can be effectively corrected by Tikhonov regularisation with GCV (see subsection 3.1).

Furthermore, systematic errors add to the above-mentioned stochastic uncertainty, and consist of centering and alignment errors of the global array as well as its deviation from the circular cross section. Clearly, the regularisation algorithm is not able to filter this type of error [6].

First, some simulations aim to show how much stochastic errors influence the reconstruction of an acoustic source. Fig. 2.8 shows the spatial averaged square error for a normal positioning error with standard deviation $\sigma_{xyz} = 3, 6, 9$ mm on each Cartesian axis. The error introduced by last two positioning inaccuracies (6 and 9 mm) starts deviating from the first case at approximately 2000 Hz. This is justified by the fact that a given positioning error has a stronger influence on a shorter wavelength. Nevertheless, the Tikhonov regularised holography gives acceptable results.

Further simulations have been carried out to investigate the effects of the three types of systematic error, *i.e.*, a global translation of the entire array of 5 mm in all the three Cartesian axes (Fig. 2.9a), an angular misalignment of 0.01 rad of the longitudinal hologram axis (max displacement of 5 mm, Fig. 2.9b), and a stretching of the circular cylinder section to an oval section (max displacement of 5 mm, Fig. 2.9c). A further simulation has been carried out for the sum of all those systematic errors. Fig. 2.10 shows the results. A part from a few

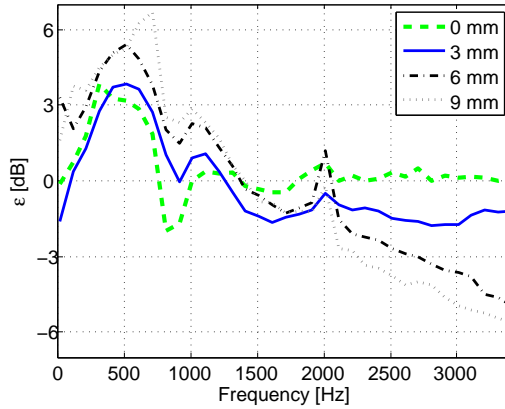


Figure 2.8: Effect of stochastic microphone positioning error for Tikhonov regularised NAH. Spatial averaged square error from 10 to 3410 Hz and step 100 Hz. The values in the legend refer to σ_{xyz} .

outliers and the high frequency range, the errors introduced by this type of inaccuracies are very small or can even be neglected.

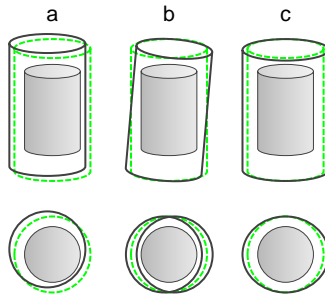


Figure 2.9: Systematic errors. Ideal holograms (dashed green) and geometric errors (solid black).

5.3.3 Measurement noise

A certain amount of noise will always affect the measurements. Two types of noise are discussed here.

The first aspect is environmental background noise. For example, an acoustic source located outside the microphone antenna may introduce a spatially correlated error which cannot be filtered by the regularisation. A typical situation is a wave reflection on a wall. Free-field conditions are needed to avoid this disturbance, which can be achieved in an anechoic room.

A further type of noise is the stochastic electronic noise of the measurement chain. Fig. 2.11 shows a set of simulations which has been performed to investigate this noise source. A normally distributed error has been added to the microphones, with a standard deviation of

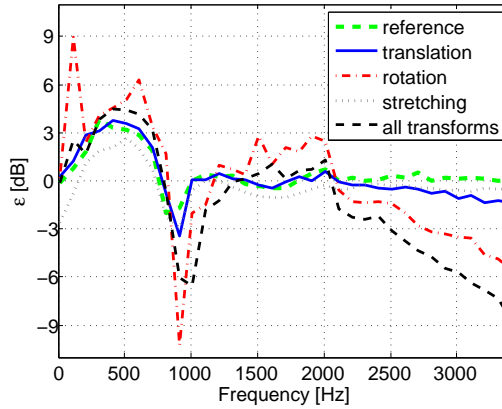


Figure 2.10: NAH spatial averaged square error regularised with Tikhonov and GCV from 10 to 3410 Hz and step 100 Hz. Effects caused by systematic errors.

0.25, 0.5, 1 and 3 dB. The figure shows that the Tikhonov regularisation can effectively filter this type of noise (it has a spatially uncorrelated shape with an extremely low magnitude).

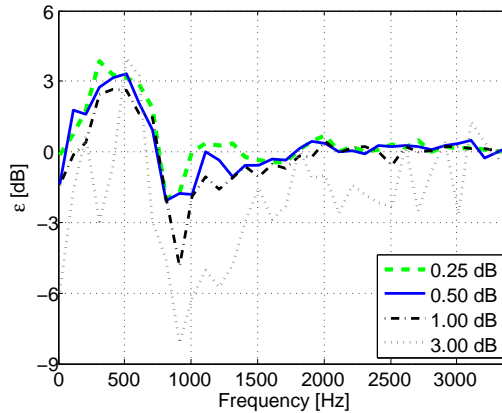


Figure 2.11: NAH spatial averaged square error regularised with Tikhonov and GCV from 10 to 3410 Hz and step 100 Hz. Effects caused by environmental noise.

6 NAH WITH COMPRESSIVE SENSING: NUMERICAL EXPERIMENTS

This section is based on reference [14], and it presents a set of numerical experiments with the aim of investigating compressive sensing within a NAH scheme.

6.1 Test case

A simplified numerical test case has been developed. The test case is one-dimensional, *i.e.*, limited to a cross section of an infinite cylinder. This implies that $k_z = 0$, which corresponds to an infinite wavelength in the longitudinal direction. Moreover, there is no spectral leakage, because the hologram consist of a circumference, along which the signal is periodic.

The dictionary is a complete (orthogonal) Fourier dictionary, built such that eq. (2.13) is satisfied. Accordingly, the source velocity profile is built by 1 or 2 Fourier components, corresponding to a sparsity of 2 and 4, respectively (each Fourier component has two complex conjugate non-zero elements). Finally, no noise is being introduced in the system, and the exact solution is sought.

The source radiates in air, and a single frequency ($f = 5000$ Hz) is considered. Two Fourier components corresponding to a circumferential order of 8 and 18 are taken into account. They refer to a propagating wave and an evanescent wave, respectively. This can be seen looking at the propagators in Fig. 2.1, which have been evaluated under the same settings.

The number of measurement points is $m = 14$, always below Nyquist-Shannon limit (order 8 would need at least 16 points). Moreover, three different sets of transducer positioning are considered. One set consist of regularly spaced microphones, while the other two sets are built from two different random distributions.

Like the example of the classical cylindrical NAH presented in section 5, the source radius is $a = 0.10$ m. Two hologram distances $d = 0.02$ m and $d = 0.04$ m are tested.

Fig. 2.12 shows the source geometry and the velocity distribution. The source consist of 42 points, regularly spaced along a circumference. Such discretization allows to propagate circumferential orders up to the 20th, as indicated by the DFT of the source velocity profile (Fig. 2.12 bottom right).

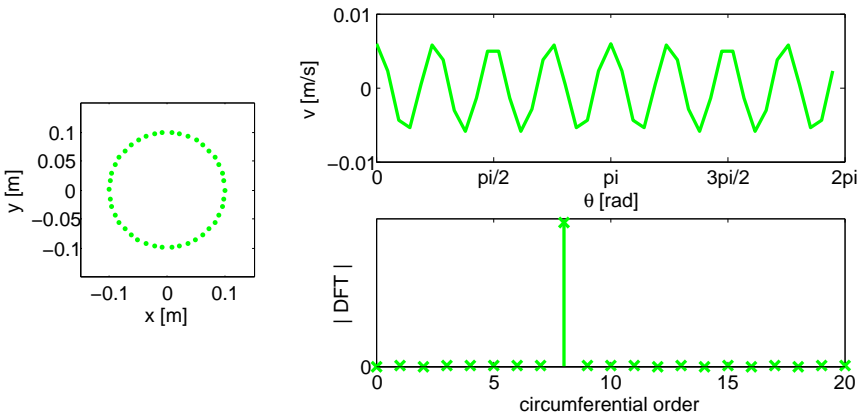


Figure 2.12: Source of the test case: geometry (left), velocity distribution (top right) and its DFT (bottom right).

Fig. 2.13 shows the microphones, according to a regular positioning (circles) and to one random scheme (diamonds), at a distance $d = 0.02$ m. A complex hologram is created starting from the source velocity profile shown in Fig. 2.12. As expected, the evanescent

order 18 is strongly attenuated.

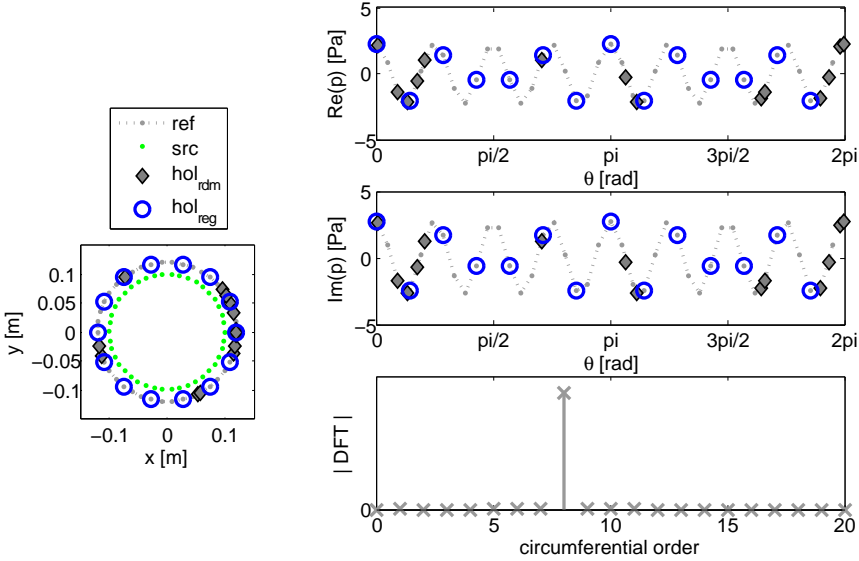


Figure 2.13: Hologram of the test case: microphone positions (left), complex hologram and its DFT (right). Legend: *ref* is the reference hologram, *i.e.*, the hologram evaluated at the 42 points that correspond to the source points, marked as *src*; *hol_{rdm}* and *hol_{reg}* are the holograms with random and regular spacing, respectively.

6.2 Simulations

6.2.1 Reference scenario

Fig. 2.14 shows the NAH results for a first simulation, which will act as reference scenario for the examples that will be described in the next subsection. Its settings are in line with Fig. 2.12 and 2.13, with the only difference that the evanescent order is omitted. Consequently, only the propagating order 8 is present (sparsity $K = 2$). It can be seen that the reconstruction of the source velocity distribution (thick dashed green) is excellent for both holograms (random and regular positioning are represented by diamonds and circles, respectively). Moreover, in this particular case basis pursuit gives the correct result also for the regularly spaced hologram with sub-Nyquist sampling.

The results have been obtained with a free MATLAB-compatible package called *cvx* [28], which allows for a fully customizable definition of problem and constraints.

6.2.2 Further scenarios

Starting from the reference scenario, three further simulation cases will be presented here.

1. Same as the reference scenario (*i.e.*, $d = 0.02$ m), but including the evanescent order 18 (such that now both orders 8 and 18 are present, with a sparsity $K = 4$). Fig. 2.15 shows again an excellent reconstruction of the velocity profile, but this time only with

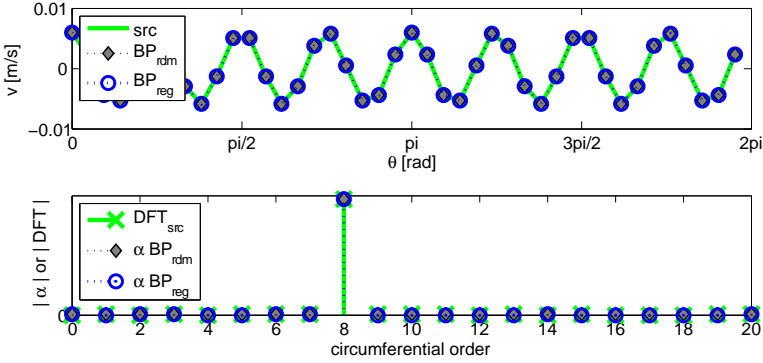


Figure 2.14: Reference scenario: reconstruction of the source velocity distribution (top) and its basis functions (bottom). Legend: src is the source, BP_{rdm} and BP_{reg} are the basis pursuit solutions with random and regular spacing, respectively; DFT_{src} is the amplitude of the source Fourier components, and α are the basis functions obtained through the basis pursuit algorithm.

the randomly spaced hologram. The failure of the regularly spaced hologram is understandable, because the number of microphones is now much below the Nyquist-Shannon limit.

2. Same as point 1 (*i.e.*, $d = 0.02$ m, orders 8 and 18, sparsity $K = 4$), but with a different random positioning. Fig. 2.16 shows that the new set does not allow for a correct source characterisation. This means that point 1 was just a “lucky case” in which basis pursuit gave the correct result.
3. Same as point 1 (*i.e.*, “lucky” random positioning, orders 8 and 18, sparsity $K = 4$), but with a higher distance $d = 0.04$ m. It is clear from Fig. 2.17 that NAH with basis pursuit failed, even if the random set is the one that has previously given the correct results. An increase in the hologram distance reduces the evanescent component substantially. At a certain point, the basis pursuit algorithm it is not able to recognize that component, even if the only noise present is extremely small (the system is affected only by numerical noise). In comparison to classical NAH, holography based on basis pursuit is more sensitive to the problem related to noise and evanescent components.

Those scenarios have been presented in order to show that indeed compressive sensing can give the correct results with less transducers, but at the same time it is extremely dangerous to rely on the solution of NAH with compressive sensing without taking care of the mathematical background, even if the sparsity of the system is very good.

7 CONCLUSIONS

The first part of this chapter gave an overview on Nearfield Acoustical Holography (NAH) in cylindrical coordinates, together with the description of a regularisation scheme. Such approach is well suited for the acoustic characterization of an electric traction motor for green mobility. Moreover, compressive sensing (CS) has been discussed as a possible tool to reduce the number of microphones required by classical NAH in the high frequency range.

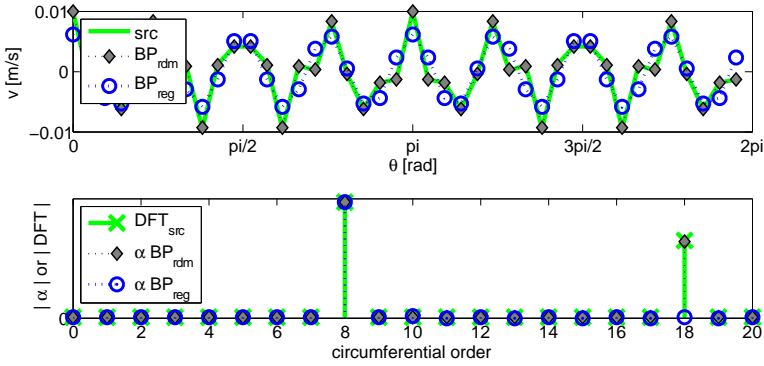


Figure 2.15: Scenario 1: reconstruction of the source velocity distribution (top) and its basis functions (bottom).

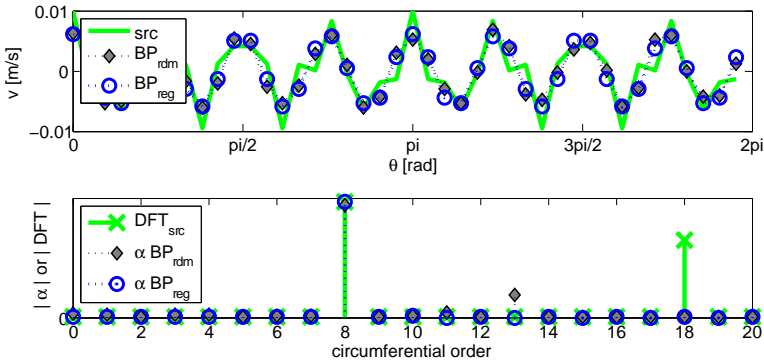


Figure 2.16: Scenario 2: reconstruction of the source velocity distribution (top) and its basis functions (bottom).

A set of numerical simulations showed a few practical aspects of classical cylindrical NAH, and confirmed the results obtained in a previous study [2, 3] for a different geometry.

The proposed antenna layout allows for microphone positioning errors up to 6 mm without introducing substantial errors ($\varepsilon \leq 3$ dB) provided the Tikhonov regularisation combined with a Generalised Cross Validation parameter selection criterion is employed.

The hologram length shall exceed the source longitudinal dimension by a factor of at least 1.5. Specifically, a hologram suitable for studying the acoustic emissions of a cylindrical source with a radius of 0.1 m and a length of 0.3 m up to a frequency of 3400 Hz is a cylindrical structure of radius 0.17 m and length 0.45 m, containing 220 microphones.

A second set of numerical simulations involved a one-dimensional numerical test-case that has been introduced in order to show the applicability of compressive sensing.

Compressive sensing relies on a matrix condition called restricted isometry property (RIP) which, unfortunately, cannot be verified for arbitrary matrices. The RIP does not hold for NAH applications, because of the structure of the matrices that build the system. In particular, the propagators of the wavenumber spectrum (k -space) deteriorate the situation, especially when the different amplification of propagating and evanescent waves becomes

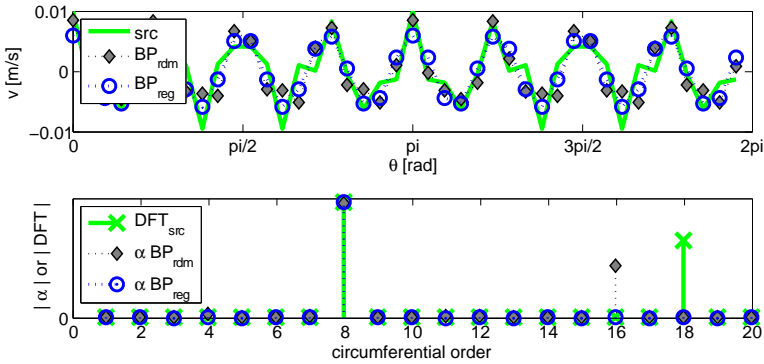


Figure 2.17: Scenario 3: reconstruction of the source velocity distribution (top) and its basis functions (bottom).

substantial. For this reason, a randomisation of the measurement positions cannot lead to a good RIP.

NAH with CS remains promising only if the sparsity of the acoustic field is sufficiently known, and this can be very problematic. To apply compressive sensing within a NAH framework, a good *a priori* knowledge of the source is needed, in order to evaluate the sparsity and enhance it by choosing the most suited dictionary.

REFERENCES

- [1] Earl G. Williams. *Fourier Acoustics: Sound Radiation and Nearfield Acoustical Holography*. Academic Press, 1999.
- [2] M. Kirchner and E. Nijman. Nearfield acoustical holography for the characterization of cylindrical sources: practical aspects. In *8th International Styrian Noise, Vibration & Harshness Congress (ISNVH 2014), Graz, Austria, 2014*.
- [3] M. Kirchner and E. Nijman. *Automotive NVH Technology*, chapter 4 – Cylindrical Nearfield Acoustical Holography: Practical Aspects and Possible Improvements, pages 47–62. SpringerBriefs in Applied Sciences and Technology – Automotive Engineering: Simulation and Validation Methods. Springer, 2016.
- [4] Finn Jacobsen and Yang Liu. Near field acoustic holography with particle velocity transducers. *The Journal of the Acoustical Society of America*, 118(5):3139–3144, 2005.
- [5] Franois Ollivier, Sylvie Le Moyne, and Christophe Picard. Experimental comparison of pu probes and microphone arrays used in impulse acoustic holography. In *Proceedings of 14th International Congress on Sound & Vibration (ICSV14), Cairns, Australia, July 9-12, 2007*.
- [6] Per Christian Hansen. *Rank-Deficient and Discrete Ill-Posed Problems: Numerical Aspects of Linear Inversion*. SIAM, 1998.

- [7] P. A. Nelson and S.H. Yoon. Estimation of acoustic source strength by inverse methods: Part i, conditioning of the inverse problem. *Journal of Sound and Vibration*, 233(4):639 – 664, 2000.
- [8] S.H. Yoon and P. A. Nelson. Estimation of acoustic source strength by inverse methods: Part ii, experimental investigation of methods for choosing regularization parameters. *Journal of Sound and Vibration*, 233(4):665 – 701, 2000.
- [9] Earl G. Williams. Regularization methods for near-field acoustical holography. *The Journal of the Acoustical Society of America*, 110(4):1976–1988, 2001.
- [10] Gilles Chardon, Laurent Daudet, Antoine Peillot, Francois Ollivier, Nancy Bertin, and Rmi Gribonval. Near-field acoustic holography using sparse regularization and compressive sampling principles. *The Journal of the Acoustical Society of America*, 132(3):1521–1534, 2012.
- [11] R.G. Baraniuk. Compressive sensing [lecture notes]. *Signal Processing Magazine, IEEE*, 24(4):118–121, July 2007.
- [12] E.J. Candes and M.B. Wakin. An introduction to compressive sampling. *Signal Processing Magazine, IEEE*, 25(2):21–30, March 2008.
- [13] Brian Hayes. The best bits. In *American Scientist*, volume 97, pages 276–280, July-August 2009.
- [14] M. Kirchner and E. Nijman. Cylindrical nearfield acoustical holography using compressive sampling: feasibility and numerical examples. In P. Sas, D. Moens, and H. Denayer, editors, *Proceedings of ISMA2014 including USD2014, Leuven, Belgium*, pages 1531–1546, 15-17 September 2014.
- [15] Scott Shaobing Chen, David L. Donoho, and Michael A. Saunders. Atomic decomposition by basis pursuit. *SIAM Rev.*, 43(1):129–159, January 2001.
- [16] E.J. Candes and T. Tao. Decoding by linear programming. *Information Theory, IEEE Transactions on*, 51(12):4203–4215, Dec 2005.
- [17] E.J. Candes, J. Romberg, and T. Tao. Robust uncertainty principles: exact signal reconstruction from highly incomplete frequency information. *Information Theory, IEEE Transactions on*, 52(2):489–509, Feb 2006.
- [18] D.L. Donoho. Compressed sensing. *Information Theory, IEEE Transactions on*, 52(4):1289–1306, April 2006.
- [19] D.L. Donoho and J. Tanner. Thresholds for the recovery of sparse solutions via l_1 minimization. In *Information Sciences and Systems, 2006 40th Annual Conference on*, pages 202–206, March 2006.
- [20] Shaobing Chen and D. Donoho. Basis pursuit. In *Signals, Systems and Computers, 1994. 1994 Conference Record of the Twenty-Eighth Asilomar Conference on*, volume 1, pages 41–44 vol.1, Oct 1994.
- [21] Emmanuel J. Candes, Justin K. Romberg, and Terence Tao. Stable signal recovery from incomplete and inaccurate measurements. *Communications on Pure and Applied Mathematics*, 59(8):1207–1223, 2006.

- [22] Emmanuel J. Candes. The restricted isometry property and its implications for compressed sensing. *Comptes Rendus Mathematique*, 346(910):589 – 592, 2008.
- [23] M. Aharon, M. Elad, and A. Bruckstein. k -svd: An algorithm for designing overcomplete dictionaries for sparse representation. *Signal Processing, IEEE Transactions on*, 54(11):4311–4322, Nov 2006.
- [24] J.M. Duarte-Carvajalino and G. Sapiro. Learning to sense sparse signals: Simultaneous sensing matrix and sparsifying dictionary optimization. *Image Processing, IEEE Transactions on*, 18(7):1395–1408, July 2009.
- [25] Yinghao Liao, Quan Xiao, Xinghao Ding, and Donghui Guo. A novel dictionary design algorithm for sparse representations. In *Computational Sciences and Optimization, 2009. CSO 2009. International Joint Conference on*, volume 1, pages 831–834, April 2009.
- [26] S. Qaisar, R.M. Bilal, W. Iqbal, M. Naureen, and Sungyoung Lee. Compressive sensing: From theory to applications, a survey. *Communications and Networks, Journal of*, 15(5):443–456, Oct 2013.
- [27] M. Ochmann. The source simulation technique for acoustic radiation problems. *Acta Acustica united with Acustica*, 81(6):512–527, 1995.
- [28] M. Grant and S. Boyd. Graph implementations for nonsmooth convex programs. In V. Blondel, S. Boyd, and H. Kimura, editors, *Recent Advances in Learning and Control*, Lecture Notes in Control and Information Sciences, pages 95–110. Springer-Verlag Limited, 2008.

Chapter 3

A Parametric Model Order Reduction for simulations of beam-based structures

ETTORE LAPPANO^{1,2,3,4}, *EUGÈNE NIJMAN*¹, *FRANK NAETS*^{2,3},
WIM DESMET^{2,3}, *DOMENICO MUNDO*⁴

¹ *VIRTUAL VEHICLE RESEARCH CENTER*

² *KU LEUVEN, DEPARTMENT OF MECHANICAL ENGINEERING*

³ *MEMBER OF FLANDERS MAKE*

⁴ *UNIVERSITY OF CALABRIA, DEPARTMENT OF MECHANICAL ENGINEERING*

1 EXECUTIVE SUMMARY

The latest advances in the field of design and optimization require new approaches to switch from component level to system level simulations. Among these new approaches, parametric Model Order Reduction (pMOR) is getting attention for its potential to solve multiphysics problems accurately and without recurring to computationally expensive co-simulation techniques.

In general, Model Order Reduction (MOR) techniques require two distinct phases; the generation of the reduced order basis (ROB) and the simulation of the reduced order model (ROM); this is a projection of the full order model (FOM) on the precomputed ROB. Parametric Model Order Reduction (pMOR) can be seen as an extension of these MOR techniques. As the most compact ROB to describe the behavior of the system is typically parameter dependent, the challenge lies in identifying a single small ROB which provides the required accuracy over the relevant parameter range.

The research discussed in this chapter investigates the possibility of applying pMOR to structural finite-element models consisting of beam elements as FOM. It is shown that for these models, the system matrices (mass and stiffness) can often be represented as an affine function of a small set of scalar parameter functions. The constituent matrices of this affine relation can be reduced offline, such that the online computational cost is independent of the FOM size. The cross-sectional and material parameters for the beams are considered in this work.

It is shown how a very efficient reduction can be performed by using a constant projection space when the manifold associated with the parameter space of interest has a small Kolmogorov n -width.

The work-flow to generate the parametric reduced order model (pROM) is as follow: parameter sample generation of the full order models (FOM); selection of the appropriate scalar parameter functions; use the FOMs to construct the local ROB (modal space) for a single parameter; generate the global ROB through an ad-hoc developed greedy algorithm. This procedure is validated numerically on a FE model of a gantry bridge. This example demonstrates the speed-up for evaluating different parameter responses from the pROM in comparison to the FOM while still maintaining the required accuracy.

2 INTRODUCTION

Integrated multi-domain design is becoming more and more relevant in industry with the increasing need in mass reduction and machine performance improvements. Finite Element method (FEM) and the other modelling techniques based on discretisation of governing (partial) differential equations of these different interacting domains often require a large number of degrees of freedom (DOF). This makes the simulations computationally expensive which is undesirable in case of dynamic studies in a multi-query context like optimization. In this regard, model order reduction (MOR) is very promising as it allows compression of the information obtained by large models without significant loss in accuracy.

MOR is often obtained via projection methods. These techniques apply to full order systems and generate the solution in 3 steps: Computation of the full order matrices, computation of the reduced order basis (ROB), projection of the full order matrices on the ROB. The solution is then obtained solving the resulting reduced order model (ROM). The ROM obtained with this procedure still depends on the size of the full order model (FOM). In fact, for different parameter configurations, different full order matrices have to be computed. Moreover, the optimal ROB (with minimum number of vectors) extracted for a specific parameter configuration can only span the subspace containing the solution for that specific configuration. All the subspaces of each parameter configuration have only one important thing in common: they are all contained in the same manifold.

The challenge is generating a ROM independent from the original size of the FOM meaning that for each parameter change, the ROM can be updated without computing the new full order matrices or a new ROB. These techniques can be called parametric model order reduction (pMOR) techniques. The new framework, by which the simulations are done, consists of two separated parts: an offline phase, where the parametric ROM is generated; online phase, where the simulation takes place and it should provide the highest computational performance possible. Performance and size of the ROM are dependent on the quality of the previously mentioned manifold. An important property of the manifold is its Kolmogorov n -width. This indicates how much the subspaces contained in the manifold vary from one to another in the parameter range of interest. In particular, if the Kolmogorov n -width is small the subspaces vary very little and they can all be spanned by the same global ROB. At local level (for the specific parameter configuration), the global ROB does not necessarily offer the maximum reduction but it provides the same required accuracy for all the parameter configurations of interest.

When the Kolmogorov n -width is large, the number of vectors required in the global ROB is large thus the resulting reduction will not be sufficient for the performance required and typically other approaches have to be employed. Interpolation methods for manifold are an

interesting field of research as there is an open challenge in trying to keep consistency of the reduced coordinates from one ROB to another [1]. Recently [2], new pMOR techniques based on partitioning of the parameter space have been developed showing interesting potential for complex nonlinear problems. In these techniques, a good balance between the accuracy of the local ROB's calculated offline and the speed of the ROB selection for the online simulation is essential. The PEBL-ROM [2] generates a partitioning of the parameter space with a bisection tree structure that gives performance advantages also in the online simulation.

The goal of this work is to develop a pMOR technique that minimizes the simulation time for FE models of beam networks by bringing all the expensive computation offline. This pMOR scheme is based on an affine representation made ad-hoc for models of beam networks and a global projection space is used considering problems of small Kolmogorov n -width. The two together allow to generate a ROM completely independent from the computational load of the original FOM.

In literature, affine functions to describe the stiffness matrix variation of a plate with the thickness are already used for pMOR. In [3], the authors use Taylor expansions to retrieve affine functions to describe the stiffness matrix variations due to thickness changes of a panel. Alternative to Taylor expansions, curve fitting with a low order polynomial can be used. In either case, the method requires very little knowledge of the system making it easy to implement. The main drawback is that the number of affine functions needed grows exponentially with the number of parameters of interest. The affine functions for describing stiffness variations are derived based on an analytical beam model. This approach decreases considerably the amount of functions needed for an accurate description and permits an accurate analysis of multi-parameter perturbations.

The chapter refers to the research presented in [4, 5] and is organized as follows. Section 3 is taken from [4] and contains a short and general overview on projection methods for MOR is given. In section 4 (from [5]), the pMOR scheme is described. In section 5 (from [5]), the affine functions of the parameters are derived based on physical considerations of the beam and are used to describe the system matrices. The developed greedy algorithm to generate the global projection space is presented in section 6 taken from [5]. In section 7, an application to a gantry-bridge for laser cutting is presented. The bridge presents a network of simple beams all characterized by a hollow rectangular cross-section. Comparisons with the results of the FE model are shown.

3 PROJECTION METHODS FOR MODEL ORDER REDUCTION

Projection methods are a basic tool used to extract approximations to the solution of large linear systems. In fact, large part of MOR techniques is projection-based [6]. This strategy has proven to be very effective as it compresses the original models with minimal loss of information.

In structural dynamics, components can be modelled as a n -DOF system through semi-discretisation in the spatial domain by means of FEM and can then be represented as a set of second order ordinary differential equations ODE:

$$Kx + C\dot{x} + M\ddot{x} = Bu \tag{3.1}$$

In this equation $K, C, M \in R^{n \times n}$ are respectively the semi- discretised stiffness, damping and mass matrices. $x \in R^n$ is the vector of nodal displacements and $B \in R^{nm}$ is the force application matrix for the m input forces u . A projection techniques is meant to extract an approximation of the solution to problem of equation (3.1) from a subspace of R^n . In general,

projection technique needs two subspaces: the projection subspace (right subspace), used to approximate the solution, and the subspace of constraints (left subspace). Thus, the vector of motion x of equation 3.1 can be expressed as a linear combination of vectors of motion (vectors used to span the projection subspace)

$$\tilde{x} = \Psi x_r \quad (3.2)$$

where $\Psi \in R^{n \times q}$ is a matrix whose columns are the vectors used for projection, vector $x_r \in R^{q \times 1}$ is the new state vector and its components are referred to as modal participation factors when a modal reduction is applied.

Equation (3.2) introduces an approximation therefore, the use of \tilde{x} into equation (3.1) brings in a residual term $r = K\tilde{x} + C\dot{\tilde{x}} + M\ddot{\tilde{x}} - Bu$. A subspace of constraints spanned by Φ is then needed such that $r \perp \Phi$. This two-sided approach is called Petrov-Galerkin projection and is an oblique projection. When $\Phi = \Psi$ the Petrov-Galerkin condition is called Galerkin condition and is said to be an orthogonal projection [6].

For the work presented in this chapter, Galerkin projection is implemented. Therefore in this text, both projection basis and ROB refer to a set of vectors that span the subspace that contain the approximation to the solution.

Projection bases can be retrieved in many ways both in the frequency and in the time domain [7, 8]. Frequency-domain techniques are well suitable for stationary problems where a small selection of reduced order basis is suitable to describe the system in a certain frequency band. For problems with strong transients, like shocks, or nonlinearities, time-domain simulations are better suited. For more detailed information about available techniques for ROB generation, the reader can see [7, 8].

4 THE REDUCTION SCHEME

Model order reduction procedures based on projection consist of distinct operations to be executed:

- (i) generation of a Full Order Model (FOM);
- (ii) generation of the global ROB;
- (iii) projection of the FOM on the subspace spanned by the ROB to generate a ROM;
- (iv) simulation of the ROM.

These operations can be executed offline (executed only once in the preprocessing) or online (executed at each calculation). The ideal configuration for optimal reduction is when operations (i-iii) are all made offline and only (iv), the simulation, is performed online. This can for example be achieved by employing a reduced basis (RB) method [5]. These methods require that the FOM can be expressed as an affine function of the parameters.

The affine representation of a general parametric matrix $A \in R^{n \times n}$ is expressed as

$$A(\mu) = \sum_{i=1}^q A_i f_i(\mu) \quad (3.3)$$

where the A_i represent the matrices of coefficient that are constant and parameter independent, and the corresponding f_i are scalar basic functions of the parameters. Given a general

parametric n degrees-of-freedom (DOF) system in matrix form without damping

$$\sum_{n=0}^p K(\mu)x + \sum_{n=0}^p M(\mu)\ddot{x} = Bu \quad (3.4)$$

where $K(\mu), M(\mu) \in R^{n \times n}$, are respectively the parametric stiffness and mass matrices, $x \in R^n$ is the vector of nodal displacements and $B \in R^{n \times m}$ is the force application matrix for the m input forces u . Using the affine representation of equation (3.3), the system matrices can then be represented as

$$\sum_{n=0}^p K_n f_n^K(\mu)x + \sum_{n=0}^p M_n f_n^M(\mu)\ddot{x} = Bu. \quad (3.5)$$

Equation 3.5, can be reduced through a Galerkin projection on the subspace spanned by the ROB indicated as $V \in R^{n \times q}$ with q generalized coordinates.

$$V^T \sum_{n=0}^p K_n f_n^K(\mu)Vx_r + V^T \sum_{n=0}^p M_n f_n^M(\mu)V\ddot{x}_r = V^T Bu. \quad (3.6)$$

Thanks to the affine representation, the projection of the constant matrices can be done offline with enhancements of the computational performance. The resulting ROM is

$$\sum_{n=0}^p K_{n,r} f_n^K(\mu)x_r + \sum_{n=0}^p M_{n,r} f_n^M(\mu)\ddot{x}_r = V^T Bu. \quad (3.7)$$

Equation (3.6) represents already a ROM but this implies that the projection of the full system matrices is performed in the online phase prior to simulation. With equation (3.7), the affine representation of the system is exploited and the constant matrices K_n and M_n of equation (3.6) can be reduced offline to generate the reduced constant matrices $K_{n,r}$ and $M_{n,r}$.

The affine representation of equation (3.3) is derived in section 5 for a framework of beam elements. The projection space V will be generated through a greedy algorithm developed ad-hoc to work with eigenvectors as described in section 6.

5 AFFINE REPRESENTATION FOR BEAMS

Projection based MOR applies to a vast range of detailed numerical models. Structural FE models will be used in this work to study the dynamics of a network of beams.

The starting hypothesis is the existence of a finite-dimensional set of functions of the parameters of interest that can describe the matrix variation. In Hong et al. [3], the variation of the stiffness of a plate with respect to one geometrical parameter is described without the need of interpolation using a Taylor polynomial. A general polynomial expansion of d variables of order η would lead to η^d monomials and in a multivariate problem, as the one herein presented, this approach results unfeasible and a different approach has to be found.

The proposed approach is to look into the mechanism of deformation of the beam element and to find the affine function of the parameters needed to describe the system matrices. The 3D beam element refers to a straight bar with uniform cross-section that can undergo axial, bending, and torsional deformation. The shape functions of a 3D beam element have to describe a few different phenomena: longitudinal displacement, axial torque, transversal

deflections and rotations. The beam element has two nodes located at its extremities, each having six DOF. Herein, linear elastic behaviour of the material is considered.

Considering the reference frame to be the three principal axes, it is convenient finding the stiffness quantities through force and moment equilibrium equations at the nodes. In fact, using this shrewdness, the stiffness matrix of a single 3D beam element is strongly decoupled and can be divided in sub-matrices [9]. The global stiffness matrix of the beam element contains all the necessary information to generate the affine functions used in the presented method.

Below, formulas describing load-displacement relations of the DOF in the 3D beam element are discussed in order to find a minimal set of basic function that can describe the relation between the design parameters and the system matrices used to simulate the system behaviour.

5.1 Axial translation and rotation

The submatrix corresponding to axial load is a 2 by 2 matrix. The entries are all proportional to

$$k_1 = EA/L \quad (3.8)$$

where, E is the young modulus, A is the cross section, L the length of the beam. The submatrix relative to the axial torsional DOF is also a 2 by 2 with entries proportional to

$$k_4 = T/\gamma = \frac{GJ}{L} \quad (3.9)$$

In this equation J is a shape factor [10] that is introduced in place of the polar moment of inertia to account of the warping of the surfaces during axial rotation of non-circular cross-sections. The dimension of this factor is $[m^4]$. This can be generally expressed as a function of the geometrical parameters that define the cross section. In [11] the expressions of J are listed for many different geometries.

5.2 Transverse deflection and rotation

The mechanism of deformation due to transverse load is a complex phenomenon that is governed by partial differential equations that not always have a known exact solution. However, in the hypothesis of small deformation, accepted approximations are available and used. These are Euler-Bernoulli beam theory, Rayleigh beam theory and Timoshenko beam theory, from least to most accurate. The first is only valid for slender beams as it does not include any effect due to shear, and rotational inertia are neglected. Rayleigh theory includes rotational inertia but this brings very little improvements as it still considers an undistorted cross-section during bending. The deflection calculated according to Timoshenko beam theory includes the effect of shear [12]. Effect of shear has to be taken into account for non-slender beams and this is of crucial importance in a FE model where, if a dense mesh is used, the characteristic length of the beam elements would result in short beams where the shear effect is dominant and cannot be neglected.

The methodology herein presented uses Timoshenko beam theory. The two mechanisms of deformation, bending and shear, can be thought to work in series. In fact, one of the fundamental hypothesis to derive this theory is that the total deflection equals the sum of the deflection due to bending and the deflection due to shear

$$d(x) = d_b(x) + d_s(x) \quad (3.10)$$

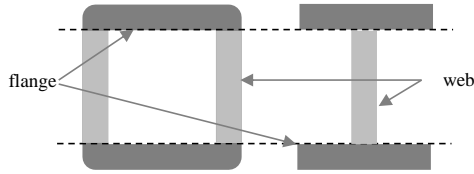


Figure 3.1: Cross-sectional surface partitioning [4]. The portions indicated as flange are those where most bending energy is absorbed. The shear is dominant in the web. The notation comes from the I-shape cross-section and it is used analogously for the hollowed rectangle cross-section [13].

where, d_b and d_s refer to bending and shear deformations respectively. To find the total deflection the two contributions are retrieved solving the following differential equations separately.

$$\frac{\partial^2 d_b}{\partial x^2} = \frac{Px}{EI} \quad (3.11)$$

Equation (3.11) relates the bending moment to the transverse displacement of the beam. I_y is the moment of inertia about y-axis.

$$\frac{\partial d_s}{\partial x} = -\frac{P}{kAG} \quad (3.12)$$

Equation (3.12) describes the relations between the shear force and the transverse displacement; k is the form factor for shear defined as

$$k = \frac{A}{I_y^2} \int_A \frac{Q^2}{b^2} dA \quad (3.13)$$

where Q is the first moment, b is the distance of the infinitesimal area dA from the neutral plane for bending. Simplifications of equation (3.13) are available for most common cross-sections. The application presented in section 7 uses hollow rectangular cross-section of which in [13] is given an approximation for the form factor

$$k = A/A_{web} \quad (3.14)$$

with A_{web} being the portion of surface as indicated in figure 3.1. Once the general solutions of the differential equations (3.11) and (3.12) are calculated, boundary conditions typically used in FE can be applied to generate the expressions of the stiffness. The sub-matrix for the transverse deflection and rotation can be written as

$$k_d = \begin{bmatrix} R & L/2 \cdot R & -R & -L/2 \cdot R \\ L/2 \cdot R & L^2/4 \cdot R + EI/L & L/2 \cdot R & L^2/4 \cdot R - EI/L \\ -R & L/2 \cdot R & R & -L/2 \cdot R \\ -L/2 \cdot R & L^2/4 \cdot R - EI/L & -L/2 \cdot R & L^2/4 \cdot R + EI/L \end{bmatrix} \quad (3.15)$$

where

$$R = \frac{12EI}{L^3} [1 + 12EI/(kAGL^2)]^{-1}. \quad (3.16)$$

5.3 The affine function

From equations (3.8 - 3.16), affine functions that can describe all the entries of the stiffness matrix (approximately) can be generated. If the parameters of interest are those of the cross-section it is possible to take all the independent expression that contain the parameters and an affine representation of the stiffness matrix can be made:

$$K(\mu) = \sum_{i=1}^q A_i f_i(\mu) \quad (3.17)$$

The A_i represent the matrices of coefficient of the corresponding basic function f_i . The parameters that can be taken into account are those that define the cross-section and the material properties. In section 7 where an example is given, elements characterized by hollow rectangular cross-sections are adopted and the parameters taken into account are h, w, t being height, width and wall thickness. Therefore, equations (3.8 - 3.16) are simplified and rewritten to generate an independent set of base functions. The chosen basic functions are summarized in table 5.3.

From affine function (3.8) and (3.8) of table 5.3, one can notice how the length of the beam is not an invariant of the problem in this case: if the system contains 2 beams of same cross-section but different length, equations (3.8) and (3.8) have to be evaluated for both lengths. However, as most beam meshes show relatively high regularity, a sufficient number of beams with the same parameters are typically present, such that a useful reduction can be obtained.

As previously mentioned, the affine representation is obtained through a LS procedure. The set of functions should be chosen numerically independent in order to limit the computational load. This can be double-checked by separating the expressions in basic monomials. The LS problem to solve is used to find the coefficient matrices A_i of equation (3.17), for each element of matrix K

$$\min(\|K_{i,j}(\mu) - F(\mu) \cdot A_{1:q}^{i,j}\|^2) \quad (3.18)$$

with μ a configuration of the parameters and $F(\mu)$ the matrix that contains the affine functions evaluated for the configuration of the parameters. It follows that a number Q of stiffness matrices coming from an FE software have to be generated. For the entry i-j the problem reduces as

$$A^{i,j} = F(\mu)^\dagger \cdot [K_{i,j}(\mu)] \quad (3.19)$$

where the symbol \dagger refers to the pseudo inverse operation. A similar procedure can be used to generate the parametric mass matrix. Suitable affine functions should be provided and the LS method should be applied. For the element with hollowed cross-section of the example in section 7 a lumped mass matrix is used therefore the resulting affine functions are

$$m_x = m_y = m_z = \rho \frac{L}{2} A \quad (3.20)$$

where ρ is the volumetric density, m_x, m_y and m_z are the 3 linear mass components. And for the rotational inertia

$$J_x = \frac{L}{2} J \quad (3.21)$$

where J is the polar moment of inertia. The mass matrix used in this work is a lumped mass matrix and this justifies the selection of base functions (3.20-3.21). In fact, it is important for accurate results that the fitting of the mass matrix is done with affine functions that are consistent with those implemented in the FE model.

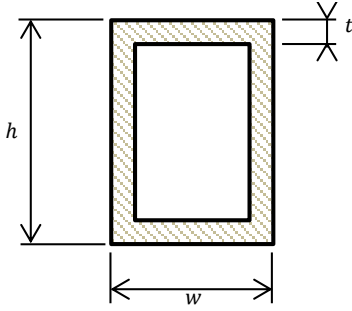
Cross-section	Affine functions	Description	#
	$A = 2(h + w)t - 4t^2$	From eq. (3.8)	1
	$J = \frac{2t^2(h-t)^2(w-t)}{(h+w)t - 2t^2}$	From eq. (3.9)	2
	$I_y = \frac{h^3w}{12} - \frac{(h-t)^3(w-t)}{12}$	From eq. (3.15)	3
	$I_z = \frac{hw^3}{12} - \frac{(h-t)(w-t)^3}{12}$	From eq. (3.15)	4
	$I_y \left[1 + \frac{12EI_y}{\ _1 AGL^2} \right]^{-1}$	From eq. (3.15)	5
	$I_z \left[1 + \frac{12EI_z}{\ _2 AGL^2} \right]^{-1}$	From eq. (3.15)	6

Table 3.1: Example of affine functions derived for a beam with hallow rectangular cross-section [4].

The scheme of equation (3.17) adds an important constraint: the full order matrices used to feed the LS method should be all of same dimensions. Therefore, parameter variations should not affect the topology of the discretisation in this case. In the following section, the parametric matrices are projected while maintaining the affine dependency.

6 THE GREEDY ALGORITHM

6.1 A general background

Greedy algorithms were introduced in the seventies as optimization techniques [14]. They increased their popularity in many field because, despite the fact they do not necessarily find a global optimal solution they succeed in finding local optima in a relatively short time [15].

In the field of MOR, greedy algorithms are used to construct subspaces adding iteratively new vectors to the basis. The objective function is the accuracy of the solution coming from the ROM therefore the method will seek where, in the parameter range of interest, the solution at iteration $q - 1$ is worst for the existent ROB V_{q-1} and add new information using the FOM. The general workflow of a greedy algorithm is the following:

- (i) selection of the parameter domain and sampling;
- (ii) initialization of the procedure with a nominal basis vector;

- (iii) employing an a posteriori error estimator to localize the combination that yields the worst result
- (iv) updating of the available set of basis vectors.

The method will iterate between (iii) and (iv) until the tolerance threshold set for the error estimator is matched. The procedure has several crucial characteristics: if N is the number of samples chosen for the ROB generation, the error estimator will be called N times per iteration. Therefore, the error estimator has to be cheap to compute and not be dependent on the complexity of the FOM.

An error estimator is an indicator of the error committed with the ROM with respect to the FOM. Error estimators are used in many MOR schemes to generate adaptively the ROB. As discussed above, the error estimator should be fast to compute as it is called many times in the ROM creation algorithm and should be asymptotically correct with respect to the actual error [15]. Given a continuous and coercive parametric variational problem, a relation between error and residual can be obtained in matrix form as

$$r(v, \mu) = Ae(v, \mu) \quad (3.22)$$

where A is the system matrix. If A is *non-singular* both sides can be pre-multiplied by A^{-1} . Calculating the norm on both sides and exploiting the triangle inequality

$$\|e\| \leq \|A^{-1}\| \cdot \|r\|. \quad (3.23)$$

This important result allows to solve the local minimization of the error using an error estimator based on the residual.

In the next session a specific error estimator to be used in the construction of ROB is presented.

6.2 The proposed greedy algorithm for eigenvector basis

The concept behind the methodology presented here follows that of RB methods. However, the error estimator has to take information from the residual of an eigenvalue problem. To ensure the generality of the method some analytical considerations are made.

Given a parameter domain of interest that is limited as $\mu_{low} \leq \mu \leq \mu_{high}$, the procedure starts choosing as initial ROB a truncated set of eigenvectors of a nominal configuration of the parameters indicated as V_0 . At each iteration i , the system is updated by a set of new vectors chosen according to the error estimator. The new ROB V_i is then obtained as the combination of the old ROB V_{i-1} and this new set of vectors.

The residual of an eigenvalue problem similarly to equation (3.22) can be expressed as

$$r = (K_i - M_i \hat{\lambda}_{ij}) \hat{X}_{ij} \quad (3.24)$$

where $\hat{\lambda}_{ij}$ and \hat{X}_{ij} come from the ROM, while K_i and M_i are the FOM matrices. If $\hat{\lambda}$ and \hat{X} are an eigenvalue and corresponding eigenvector for the problem of equation (3.24), the residual term will be zero. In the general case, $\hat{\lambda}$ and \hat{X} are not expected to be a solution of equation (3.24) therefore a residual $r \neq 0$ is obtained. From equation (3.24) it is not straight forward to invert and obtain an error bound as it is in equation (3.23). In fact equation (3.24) has two error source and requires finer considerations: for very accurate approximation of the eigenvectors the residual may still be very high if the paired approximated eigenvalue

is far from the actual eigenvalue. Vice versa, having a precise eigenvalue, therefore a small residual, does not necessarily guarantee a good approximation for the eigenvector.

Proving that the residual of equation (3.24) can be used as error estimator for a greedy algorithm is possible introducing the theory on matrix perturbations. Investigations on eigenvalue and eigenvector sensitivity due to matrix perturbation are particularly relevant for the scope of this work [16].

The accuracy of the approximated eigenvalues depends on the conditioning of the diagonalisation matrix. If this results ill-conditioned, the residual norm will not represent a thoroughly trustable error estimator. This is formalized in a theorem proved in [16] that is here recalled.

Theorem 1. Given a semisimple matrix $A \in C^{m \times n}$, suppose $V^{-1}AV = D$, where D is a diagonal matrix and V is non-singular. Given a perturbation of the matrix δA , $\hat{\lambda}$ is an eigenvalue of the matrix $A + \delta A$. It follows that A has an eigenvalue λ such that

$$|\hat{\lambda} - \lambda| \leq \text{cond}(V) \|\delta A\|_p \tag{3.25}$$

where $\text{cond}(V)$ represents the condition number of the matrix V and $\|\cdot\|_p$ represents the p-norm and $p \leq \text{inf}$. This tells that, the approximation of the eigenvalues is good if the condition number of the matrix of eigenvectors V is good and the perturbation of the system A is small. The other requirement is on the eigenvectors whose sensitivity assessment results to be more complex. A condition number for eigenvectors can be obtained using a Schur-like decomposition of the system (see chapter 6 of [16]). A condition number estimator for the eigenvectors is just given by the quantity $\|A^{-1}\|$.

Table 6.2 shows the greedy algorithm proposed. To favor readability the error estimation is here based on only one eigenvalue pair but the essence of the algorithm does not change if the estimate is done using more pairs. The matrices K_i and M_i may be large depending on the complexity of the model. Therefore it is convenient precomputing them as this will bring important improvements of computational costs also in the preprocessing time. Unlike other greedy approaches present in literature where a single vector contribution per iteration is usually added, this procedure requires to add a set of vectors at each iteration. This is done to improve the convergence of the method. The added set corresponds to the parameter configuration whose largest amount of information is missing. The drawback of adding a set of vector is that some of the information spanned by the added vectors is probably already available in the temporary global ROB and has to be filtered out. Therefore, the union operation of line 12 is done through SVD. The algorithm of table 1 is implemented and discussed in the numerical example of section 7.

7 STUDY CASE

This section shows an application of the developed pMOR scheme to a gantry crane for laser cutting. Gantry refers to a bridge-like structure that can be used for moving objects over an area or for performing planar machining operation. Therefore, a gantry should be designed according to the excitations, the velocity of operations and the weight to be carried during the operations. The initial design of the gantry is shown in figure 3.2. A combination of high-speed manoeuvres and heavy loading may cause the entire structure to malfunction or resonate.

The main components of this gantry are a bridge, two motors, and a laser head (figure (3.2)). The bridge is attached to a railway and is modelled as a truss; it is expected to be the most sensitive to the large accelerations of the manufacturing process. Therefore, the system

```

1: Function  $\mathbf{V}_g = GreedyAlgorithm(\mu, \mathbf{V}_{\mu_0}, toll)$ 
2:  $\mathbf{V}_g = \mathbf{V}_{\mu_0}$ 
3: while  $MaxR > toll$ 
4: for  $i = 1 : N$ 
5:  $[K_i, M_i] = getFOMmatrices(\mu_i)$ 
6:  $K_r = V_g^T K_i V_g$ ;  $M_r = V_g^T M_i V_g$ 
7:  $[X_r, \lambda_r] = eig(K_r, M_r, 1^{st} mode)$ 
8:  $r_i = K_i V_g X_r - M_i V_g X_r \lambda_r$ 
9: end for
10:  $[MaxR, ID] = max(r)$ 
11:  $[V(\mu_I D), \sim] = eig(K, M)_{(\mu_I D)}$ 
12:  $\mathbf{V}_g = V_g V(\mu_I D)$ 
13: end while
14: end function

```

Table 3.2. Greedy approach based on the residual of one eigenvector [5].

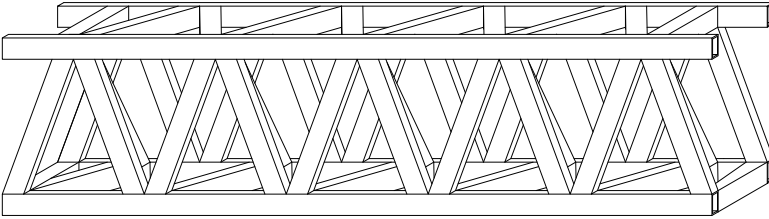


Figure 3.2. Gantry bridge of the laser-cutting machine [4].

is described as a network of beams to which lumped mass and stiffness are attached where motors and laser head are located.

If materials and topology of the structure are already selected, optimization and analysis of dynamic characteristics concern the cross-sections of the beams only. In this model, 3 cross-sections are used to model the different trusses (figure 3.3) and they are assembled in a way to ensure good compatibility for welding. There is a rectangular cross section described by h , w and 2 other squared cross-sections one of edge h and one of edge w . All beams are hollow and the wall thickness is t . The material is assumed steel and the structure is constrained in four nodes allowing only translation along the rails (y -axis).

7.1 Preprocessing and detailed parametric model generation

The gantry is modelled using 1836 DOF and the matrices are generated using NX Nastran. As discussed in section 5.3, the parameter variation should not affect the mesh topology; the number of elements and their connectivity should not change between one configuration and the other.

The equations listed in table 5.3 are rearranged and simplified according to the parameters of interest to generate the set of independent affine functions. It was mentioned that if the gathered functions contain redundant information, numerical issues might occur resulting

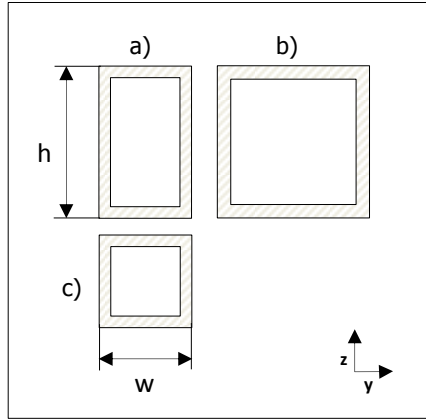


Figure 3.3. Gantry bridge of the laser-cutting machine [4].

in poor quality of the result. An example of this issue is given here considering the cross-sectional areas adopted in the truss: being A_R, A_H, A_W cross-sectional rectangle, square of edge h and square of edge w respectively.

Original functions	Independent functions
$A_R = 2(ht + wt - 2t^2)$ $A_H = 4(th - t^2)$ $A_W = 4(tw - t^2)$	$th \quad tw \quad t^2$

Table 3.3. List of functions retrieved according to 5.3 and derived unique monomials [4].

One may notice that for small wall-thickness with respect to the other dimensions, they are numerically linearly dependent and they reduce to

$$A_R \approx 1/2A_H + 1/2A_W.$$

The issue is solved by making the monomial decomposition of the three functions (table 3.3) as discussed in section 5.3.

When the set of basic functions is complete, the sampling has to be done in order to apply the LS method. The result of the LS method provides the matrices of coefficients for the affine representation of the model as in equation (3.17). The affine model is generated using a high number of sampling points and gives good results in terms of accuracy as shown in figure 3.4 where, a collocated frequency response function (FRF) at the left motor is shown.

7.2 PMOR using the greedy algorithm

The greedy algorithm presented in section 6 yields the required accuracy in 8 iterations. The resulting ROB counts 195 generalized coordinates. In figure 3.5, the representation of the sample points selected through the greedy algorithm is given.

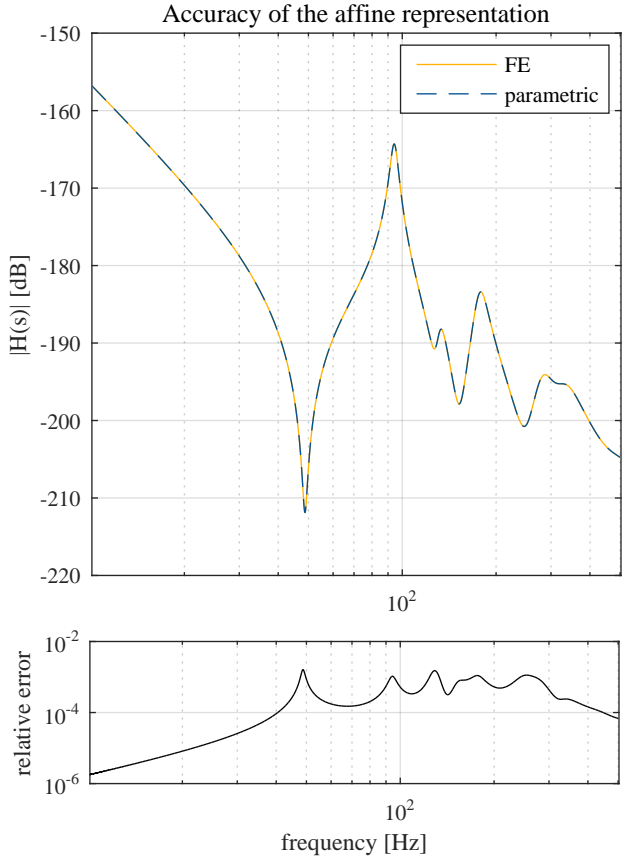


Figure 3.4: Configuration of the motor. Collocated FRF. The representation is split in two. Above the Transfer Function (TF) obtained with the matrices of Nastran is plotted with the TF obtained with the unreduced parametric mode [4].

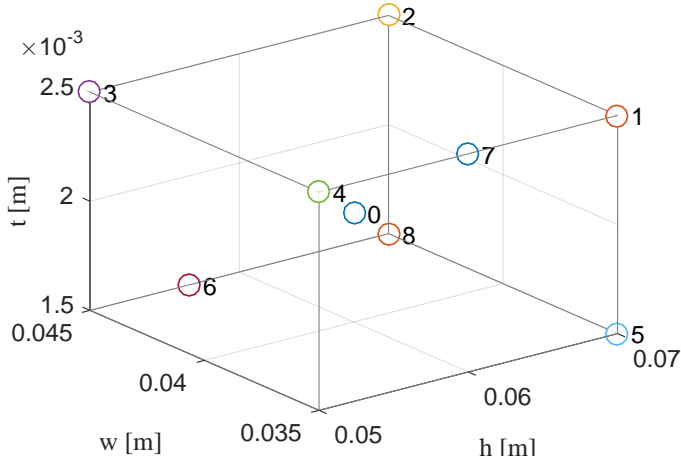


Figure 3.5: The prism represents the parameter domain that is gridded and used to construct the global ROB through the greedy algorithm presented in section 6. The enumerated points represent the parameter configuration selected by the greedy algorithm at each iteration [5].

To assess the reduction accuracy, a number of parameter configurations is taken and compared with the result of the full order model. In figure 3.6 the decay of the residual and of the actual error are plotted in logarithmic scale. Although the results seem very promising, it should be underlined that, the error in figure 3.6 only accounts for the error committed on the eigenvalue and not the error on the eigenvectors. Figure 3.7 shows the collocated frequency response functions for the load case described and for all the parameters of the model; the smooth variation of the response functions with the parameters is a good indication of a small Kolmogorov n -width for the manifold associated with the problem. Finally in Figure 3.8, the error between the FRFs computed with the ROM and the FOM are plotted.

The good results for eigenvalues of Figure 3.6 could be expected as they are aligned with the theoretical discussion of section 6.2. Nevertheless, the error representation of Figure 3.8 shows that also the FRF can be represented very accurately in the chosen parameter range.

7.3 Conclusions

In this chapter, a methodology for parametric model order reduction (pMOR) of a FE model consisting of beam elements is presented. The method consists of two parts; in the first, an affine representation of the FE model, based on mechanics of material and beam theory, is retrieved; in the second part, a global ROB is generated using an originally developed greedy algorithm based on normal modes for the parameter range to be investigated. The size of the resulting parametric ROM is completely independent from the size of the original model and, if the problem to be investigated presents a small Kolmogorov n -width, good trade-off between accuracy and reduction is obtainable.

An important benefit of the presented methodology is the capability of accounting for multi-parameter variations during simulation, without recurring to expensive interpolations of the FE model or generic polynomials of high order, because both interpolations of the FE and generic polynomials scale badly with the number of parameters. Moreover, a general set of polynomial functions might bring numerical issue in the implementation of the LS method

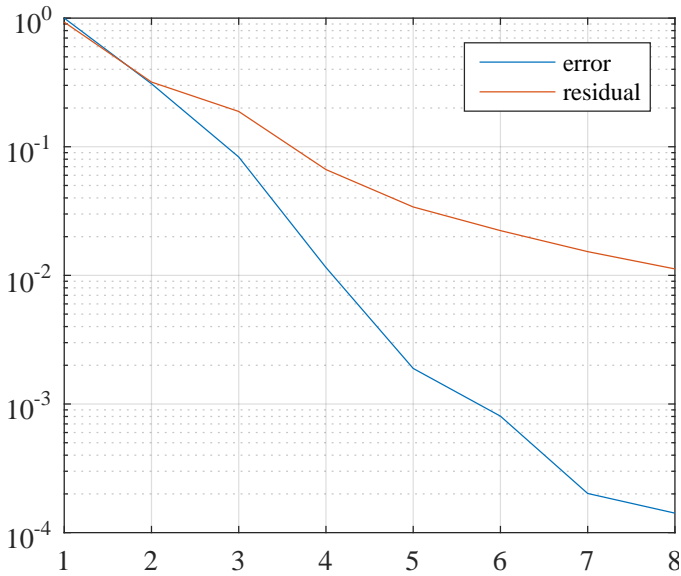


Figure 3.6. Normalized value of the actual error and of the residual at each iteration [5].

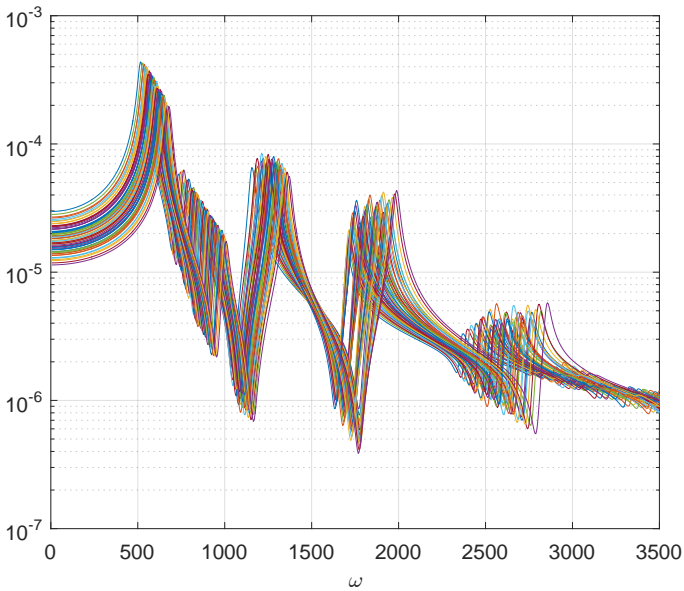


Figure 3.7: Collocated frequency response functions of the gantry bridge at the centre point where the load is imposed. Each response function line is generate using the ROM and corresponds to a different parameter configuration in the range of interest [5].

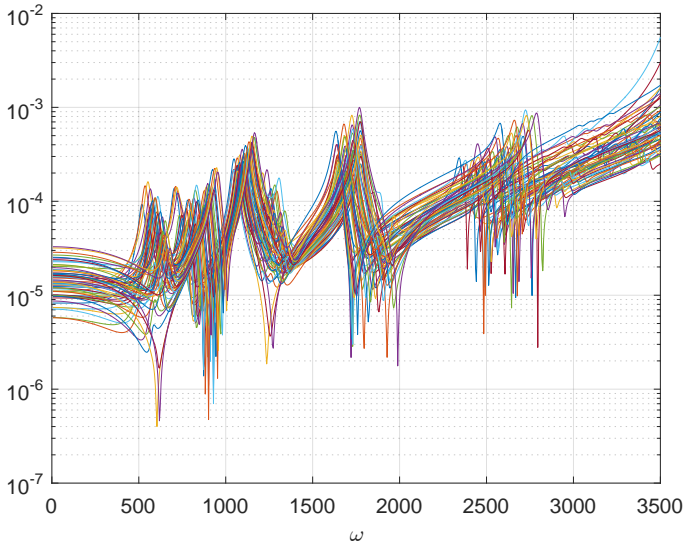


Figure 3.8: Error distribution for the FRFs plotted in figure 3.7. $e(\omega) = \left| \frac{y_{ROM}(\omega) - y_{FOM}(\omega)}{y_{FOM}(\omega)} \right|$ [5].

employed in this work.

The error estimator developed in section 6 allows an interesting implementation of the greedy algorithm when eigenvector basis are used. In fact, the greedy approach to construct the basis offers some accuracy estimation before simulation otherwise unavailable for purely modal basis. Therefore, the proposed methodology sums up the advantages of incremental improvements offered by the greedy algorithm to the popular modal reduction techniques.

Some of the theoretical investigations made through the chapter have been further analysed by means of the numerical example reflecting the potential of the methodology. Nevertheless, a number of further improvements will be presented in future research. The temporary global ROB is updated with a full local ROB at each iteration of the greedy regardless of the fact that not all the new vectors being added may be needed to improve the solution. Including only the strictly necessary vectors would allow a finer optimization of the number of generalized coordinates with improvements in memory management and performances of the simulation.

REFERENCES

- [1] David Amsallem and Charbel Farhat. An online method for interpolating linear parametric reduced order models. *SIAM Journal on Applied Dynamical Systems*, 2011.
- [2] David Amsallem and Bernard Haasdonk. Pebl-rom: Projection-error based local reduced-order models. *Advanced Modeling and Simulation in Engineering Science*, 2016.

- [3] Sung Kwon Hong, Bogdan I. Epureanu, and Matthew P. Castanier. Next-generation parametric reduced-order models. *Mechanical Systems and Signal Processing*, 37:403–421, 2013.
- [4] Ettore Lappano, Frank Naets, Martijn Vermaut, Wim Desmet, and Domenico Mundo. Development of a parametric model order reduction technique for beam-based structures. In *9th International Styrian Noise, Vibration and Harshness Congress*, 2016.
- [5] Ettore Lappano, Frank Naets, Wim Desmet, Domenico Mundo, and Eugene Nijman. A greedy sampling approach for the reduced order basis construction for structural dynamics models. In *ISMA - International conference on Noise and Vibration Engineering*, 2016.
- [6] Yousef Saad. *Iterative methods for sparse linear systems*. the Society for Industrial and Applied Mathematics, 2003.
- [7] Frank Naets. *Development of system-level model reduction techniques for flexible multibody simulation*. PhD thesis, KU Leuven, 2013.
- [8] B. Besselink, U. Tabak, A. Lutowska, N. van de Wouw, H. Nijmeijr, D. J. Rixen, M. E. Hochstenbach, and W. H. A. Schilders. A comparison of model reduction techniques from structural dynamics, numerical mathematics and systems and control. *Journal of Sound and Vibration*, 2013.
- [9] J. S. Przemieniecki. *Theory of Matrix Structural Analysis*. McGraw-hill, 1968.
- [10] Stephen Timoshenko and J. N. Goodier. *Theory of Elastic Stability*. McGraw-hill, 1963.
- [11] Warren C. Young and Richard G. Budynas. *Roarks's Formulas for Stress and Strain*. McGraw-hill, 2002.
- [12] A. Labuschagne, N. F. J. van Rensburg, and A. J. van der Merwe. Comparison of linear beam theories. *Mathematical and Computer Modelling*, 2009.
- [13] James M. Gere and Stephen Timoshenko. *Mechanics of Materials*. PWS Publishing company, 1997.
- [14] Jack Edmonds. Matroids and the greedy algorithm. *Mathematical Programming*, 1971.
- [15] Alfio Quarteroni, Andrea Manzoni, and Federico Negri. *Reduced Basis Methods for Partial Differential Equations*. Springer, 2016.
- [16] David S. Watkins. *Fundamentals of Matrix Computations*. Wiley and Sons, 2002.

Chapter 4

Equivalent modelling of sandwich beams

SOPHIE DE RIJK, EUGÈNE NIJMAN

VIRTUAL VEHICLE RESEARCH CENTER

1 EXECUTIVE SUMMARY

The main findings of ESR4 are detailed in the journal article: Equivalent material modelling of sandwich beams, evanescent solutions and damping investigations which has been accepted for publication in the Elsevier Journal of Sound and Vibrations, as of June 2016 [1]. In this chapter, the main principles and findings of the method developed by the fellow during the eLiQuiD project are shown.

2 INTRODUCTION

As legal and public pressure is increasing for having fuel efficient vehicles, engineers are pushed to design lighter structures. To reach lightweighting targets, the use of sandwich structures is one of the paths under investigation by automobile, train or aerospace industries. Such multi-material structures however bring along new challenges in terms of modelling, especially in the dynamic range. The multiple mechanisms involved in the vibrations propagation and damping in such structures require good understanding and, in term, sensible and computationally efficient modelling techniques. As a multilayered system, sandwich structures quickly become very demanding in computing power for numerical dynamic simulations, for instance with Finite Element Analysis (FEA). Having faster modelling techniques would allow to iterate more easily and efficiently on designs of structures based on simulation results. As a response to this need, the idea has risen in the literature to model multilayered systems with a single equivalent material by matching the propagating part of the solution and, in most cases, considering simply supported boundary conditions for which the eigenfrequencies are sought to be matched. The study performed here however showed that the evanescent part of the transverse vibrations solution, which represent local deformations at the structure's boundaries, are of importance to properly represent the loads at the boundaries. The boundary loads are necessary to model the transmission of vibrations between the

various parts of a structure. Another subject that was addressed is the modelling of damping in the structure, which in turn, also depends on the deformation fields at the boundaries. The research performed has focussed on using Timoshenko beam theory (first order shear theory for beams) for the equivalent modelling of transverse vibrations.

The fellow first sought for the current knowledge on the dynamics of sandwich and Timoshenko beams, shear stiffness of laminates and damping. Based on that knowledge, a new methodology was developed to construct an equivalent Timoshenko beam to represent a sandwich beam. This new methodology includes updated evanescent field considerations, shear stiffness description and damping modelling. The performance of the new model was then thoroughly studied through various analytical examples and the specific advantages and limitations of the methodology recorded, described and interpreted. Experimental measurements were also conducted on a reference case and compared to the model's predictions. The assessment of the accuracy of the model was based on comparing the location of eigenfrequencies and the width of the peaks in the frequency responses computed for the modelled and measured beams.

3 STATE OF THE ART OF SANDWICH BEAMS DYNAMICS

During the study conducted, the reference theory describing undamped sandwich structures used was that of Nilsson and Nilsson [2]. This theory considers the total bending stiffness of the layup D_{tot} , the transverse shear stiffness of the core D_s and the individual bending stiffness of the face sheets about their own mid plane D_f . The rotary and transverse inertias, I_ρ and μ are also included.

The governing equations are then given by:

$$-D_s \left(\frac{\partial^2 W}{\partial x^2} - \frac{\partial \psi}{\partial x} \right) + 2D_f \left(\frac{\partial^4 W}{\partial x^4} - \frac{\partial^3 \psi}{\partial x^3} \right) + \mu \frac{\partial^2 W}{\partial t^2} = 0 \quad (4.1)$$

$$-D_{tot} \frac{\partial^2 \psi}{\partial x^2} + 2D_f \left(\frac{\partial^3 W}{\partial x^3} - \frac{\partial^2 \psi}{\partial x^2} \right) - D_s \left(\frac{\partial W}{\partial x} - \psi \right) + I_\rho \frac{\partial^2 \psi}{\partial t^2} = 0 \quad (4.2)$$

W is the deflection of the beam and ψ the angle of rotation of the cross section about the sandwich's neutral axis.

Based on these governing equations, Nilsson and Nilsson derive the dispersion equation:

$$2D_f \kappa_x^6 + \left(D_s - 2 \frac{D_f}{D_{tot}} I_\rho \omega^2 \right) \kappa_x^4 + \left(\mu + 2 \frac{D_f}{D_{tot}} \mu + \frac{I_\rho D_s}{D_{tot}} \right) \kappa_x^2 \omega^2 - \frac{\mu D_s}{D_{tot}} \omega^2 + \frac{I_\rho \mu}{D_{tot}} \omega^4 = 0 \quad (4.3)$$

3 separate solutions for the wavenumber κ_x can be obtained from the dispersion relation in Eq. (4.3). The first wavenumber solution κ_1 represents the propagating solution. At low frequencies, it represents pure bending, at mid-frequencies shearing and at higher frequencies the individual bending of the face sheets about their own mid plane. The second wavenumber κ_2 , is composed of an evanescent solution at low frequencies and a propagating solution beyond a limit frequency f_{lim} given by:

$$f_{lim} = \frac{1}{2\pi} \sqrt{\frac{D_s}{I_\rho}} \quad (4.4)$$

Below the limit frequency (4.4) κ_2 gives a slowly decaying evanescent solution composed of a superposition of total bending and core shearing. Above the limit frequency, κ_2 gives the anti-phase superposition of total bending and shearing in the core. This superposition gives no transverse motion of the beam but can be seen as the rotation of the cross sections and local tension-compression in the face sheets. The third wavenumber κ_3 solution is a short decay exponential solution comprising bending and shearing. Figure 4.1 shows the various wavenumber solutions for a 15 mm thick aluminium sandwich beam with 1 mm face sheets.

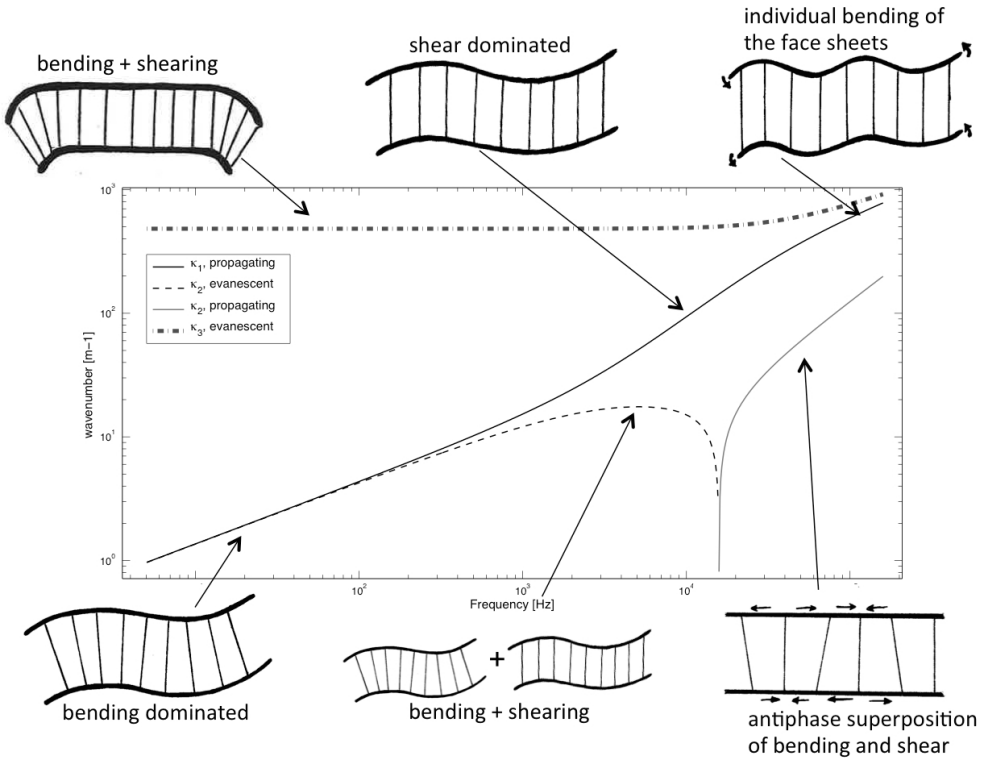


Figure 4.1: Solutions to the dispersion relation following Nilsson and Nilsson [2] with associated deformations of a 15 mm thick aluminium sandwich beam with 1 mm face sheets [1].

A visualisation of the deformation generated by each part of the dispersion can be obtained by decomposing the total deflection and rotation of the sandwich beam into the terms associated to the individual wavenumber solutions as illustrated in Figure 4.1

4 EQUIVALENT MATERIAL MODEL

As the equivalent model is meant to be used for accelerating FEA simulations, the availability of elements following the chosen beam theory for the model is an important factor. Timoshenko beam theory is used in shell elements commonly available in commercial FEA packages but still integrates considerations such as transverse shear and rotary inertia, which are important for describing sandwich beams. Therefore, Timoshenko was deemed a reason-

able choice of theory to use for our equivalent model of a sandwich beam, which itself is assumed to follow Nilsson and Nilsson’s [2] governing equations. The governing equations for a Timoshenko beam are given by [3]:

$$-D_{st} \left(\frac{\partial^2 W}{\partial x^2} - \frac{\partial \psi}{\partial x} \right) + \mu_t \frac{\partial^2 W}{\partial t^2} = 0 \tag{4.5}$$

$$-D_{bt} \frac{\partial^2 \psi}{\partial x^2} - D_{st} \left(\frac{\partial W}{\partial x} - \psi \right) + I_{\rho t} \frac{\partial^2 \psi}{\partial t^2} = 0 \tag{4.6}$$

Which yields a 4th order dispersion equation:

$$D_{st} \kappa_x^4 - \left(\mu_t + I_{\rho t} \frac{D_{st}}{D_{bt}} \right) \kappa_x^2 \omega^2 - \mu_t \frac{D_{st}}{D_{bt}} \omega^2 + \frac{I_{\rho t} \mu_t}{D_{bt}} \omega^4 = 0 \tag{4.7}$$

where μ_t is the mass per unit length, $I_{\rho t}$ the rotary inertia, D_{st} is the transverse shear stiffness and D_{bt} the bending stiffness.

The equivalent material’s Young’s modulus, shear modulus and density were then chosen to match the mass per unit length, transverse shear stiffness and bending stiffness term of the sandwich material. One of the novelties of this study was to introduce an equivalent beam’s thickness other than the total sandwich thickness in order to match the rotary inertia term and hence the second wavenumber solution κ_2 as shown in Figure 4.2:

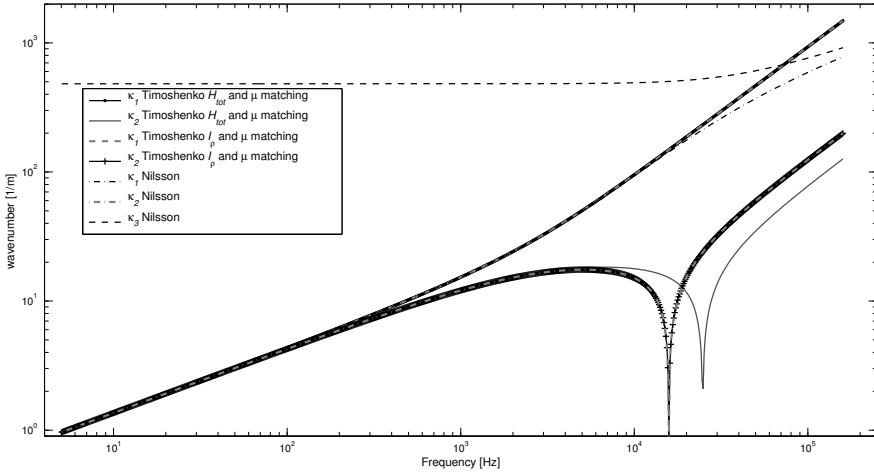


Figure 4.2: Dispersion solutions for a 15 mm aluminium honeycomb sandwich beam with 1 mm face sheets compared to equivalent Timoshenko solutions either matching H_{tot} and μ or I_{ρ} and μ [1].

4.1 Transverse shear stress distribution and correction factors

Shear stress distributions in sandwich beam structures can be quite complex and cause warping of the cross sections. In first order shear theory, this is simplified by considering a uniform stress distribution corrected by a shear correction factor. Nilsson’s theory [2], only considers the shear stiffness of the core and no shear correction factor is used to account for warping.

A shear correction factor was added to the methodology developed here. This shear correction factor was however a simplified static correction factor as the reality in the dynamic range is far more complex due to rotary inertia effects. Maheri and Adams [4] for instance have shown that the dynamic shear correction factor is frequency and boundary condition dependent. As the aim of the research was to develop a method as generic as possible for acceptable complexity, only a static shear correction factor was used, expecting that significant deviations would only appear in the higher frequency range. The newly considered shear stiffness includes the shear stiffness of the face sheets, to cover cases where the latter are not of negligible thickness and a global shear correction factor κ_s was computed following the method presented in [5]. The shear stiffness can also be expressed separately for the facesheets and the core with their respective correction factors:

$$\kappa_s \sum_{i=1}^3 G_i h_i = \sum_{i=1}^3 \kappa_{si} G_i h_i \quad (4.8)$$

with G_i , h_i and κ_{si} the shear modulus, the thickness and the shear correction factor of each layer respectively.

This approach was used to distinguish the contributions of each layers to later quantify their respective effect on global damping of the structure.

4.2 Damping

Determining the damping in the sandwich layup and applying it to its equivalent Timoshenko beam was one of the key points of the research. In FEA, damping is applied with a single loss factor η in the form of $E_t = E_t^* (1 + i\eta_{tot})$ and $G_t = G_t^* (1 + i\eta_{tot})$, E_t^* and G_t^* are the undamped moduli. A single equivalent loss factor therefore needed to be defined based on the different loss factors of the face sheets and the core. The method presented by [6] was used to compute the total loss factor as the ratio between dissipated energy and potential strain energy.

$$\eta_{tot} = \frac{E_{diss}}{2\pi E_{pot}} \quad (4.9)$$

The dissipative parts of the motion considered were the elongation in the face sheets due to bending and the transverse shearing in the face sheets and core.

5 ANALYTICAL PERFORMANCE EVALUATION

The performance of the model was then assessed with analytical examples. Two sandwich beams of total thickness of 30 mm were studied. The aluminium face sheets were of 1 mm or 5 mm thickness. The cores were aluminium honeycombs. The first example represented a typical case. The second was a limit case with high relative importance of the D_f term to show the limits of the equivalent Timoshenko beam model. Two different ways of accounting for damping were implemented in the equivalent material. The first, which is only possible analytically, considered the damping in the face sheets and the core separately. The second, which was representative of what one would do in FEA, used a single damping coefficient for the full system. This was done to better assess the accuracy of the model from the undamped and the damped point of view. The input mobilities of the Nilsson [2] sandwich beam and the equivalent Timoshenko beam model were then compared as shown in Figure 4.3.

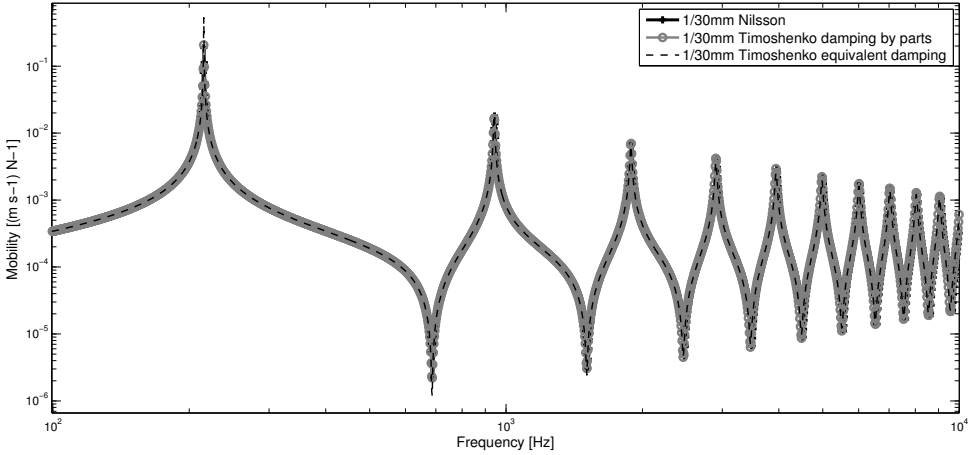


Figure 4.3: Input mobility for 30 mm thick sandwich beams with 1 mm face sheets and its equivalent Timoshenko beams [1].

The various types of motions and deformations (total deflections (W), the total cross section rotations (ψ) and the shear angle (γ)) were then decomposed by wavenumber solution contributions at chosen resonances to better understand the differences between the reference sandwich model and equivalent material model as shown in Figure 4.4.

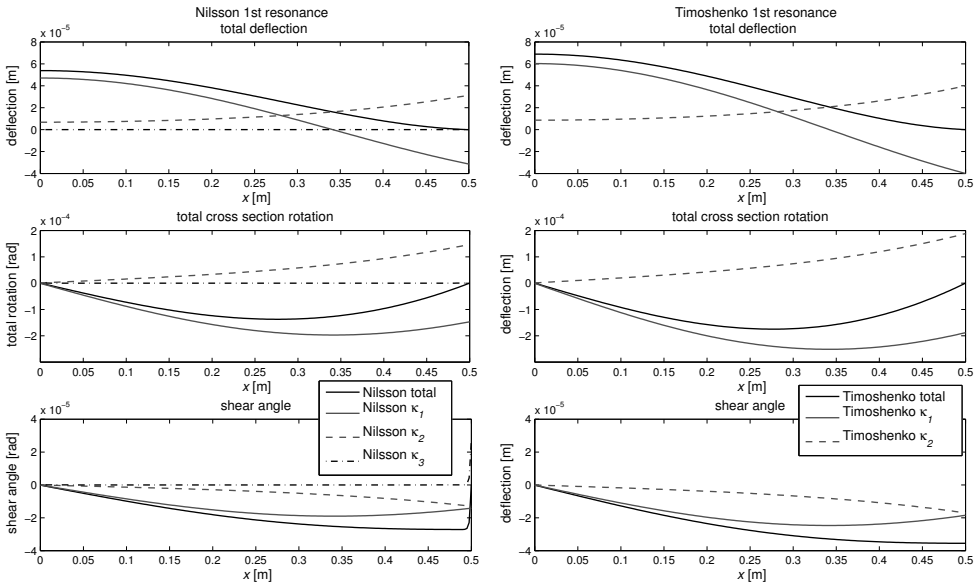


Figure 4.4: Deflection W , total rotation ψ and shear angle γ for a 30 mm thick sandwich beam modelled using Nilsson's theory or as a Timoshenko beam, 1 mm face sheets at its 1st resonance [1].

6 EXPERIMENTAL STUDY

Experimental investigations were made on a 30 mm thick sandwich beam. The face sheets were 1 mm thick aluminium sheets, the core is an aluminium honeycomb. The beam was excited at one end with an impact hammer and the velocity response were measured at the other end thanks to a laser vibrometer as depicted in Figure 4.5. The beam was placed on soft foam blocs in two points for support.



Figure 4.5: Experimental setup with a 30 mm aluminium sandwich beam supported on foam pads, excited by impact hammer and the velocity response measured by means of a laser vibrometer [1].

As the measured sandwich beam had a rather thick bonding layer between the face sheets and the honeycomb core, the equivalent material model was updated to include the effect of this bonding layer both in stiffness and damping. The experimental results were then compared to a detailed FE model to verify the accuracy of the estimated material properties of the various components of the layup, Nilsson sandwich analytical models and equivalent Timoshenko models as shown in Figure 4.6.

7 GENERAL CONCLUSIONS

The first main observation was that the evanescent parts of the dispersion solutions, which were not considered by researchers in the past, actually had a visible influence on the beam's solutions and needed indeed to be considered to construct equivalent material models. Secondly, it was shown that it was possible to construct a single equivalent damping coefficient for a sandwich beam, provided it is frequency dependent. The experimental work mainly showed the importance of considering the influence of the bonding layer between the face sheets and the core to construct an accurate model. Generally, it was shown that despite the analysed limitations of the developed model, the results of both the analytical and experimen-

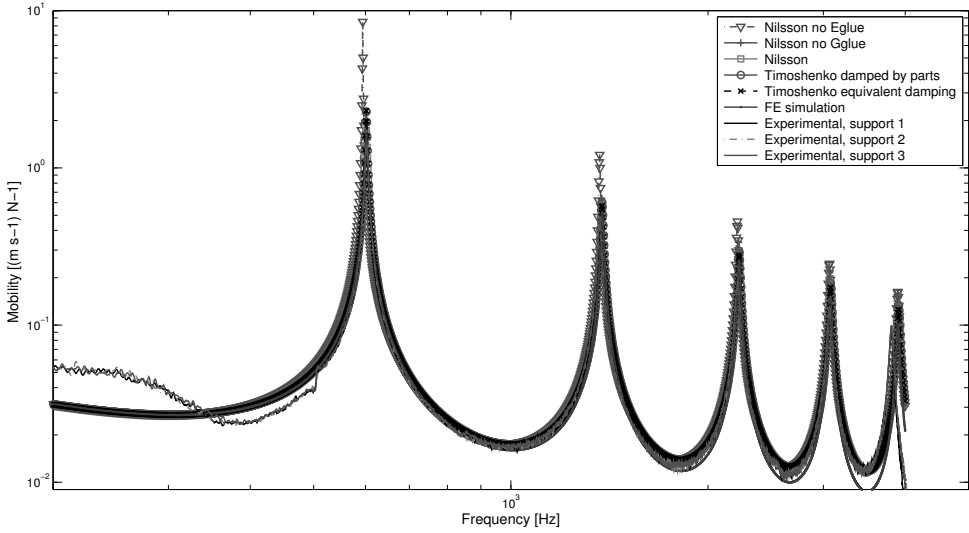


Figure 4.6: Transfer mobility of a 30 mm thick aluminium sandwich beam, following Nilsson's equations (considering the bonding layer for bending stiffness and damping, for shear stiffness and damping or both), as an equivalent Timoshenko beam damped by parts or with equivalent damping and experimentally with three different foam support pad positions [1].

tal studies proved to be very promising for using such an approach practically.

REFERENCES

- [1] S. de Rijk and E. Nijman. Equivalent material modelling of sandwich beams, evanescent solutions and damping investigations. *Journal of Sound and Vibration*, 2016.
- [2] E. Nilsson and A. Nilsson. Prediction and measurement of some dynamic properties of sandwich structures with honeycomb and foam cores. *Journal of Sound and Vibration*, 251(3):409–430, 2002.
- [3] S. P. Timoshenko. On the correction for shear of the differential equation for transverse vibrations of prismatic beams. *Philosophical Magazine*, 41(245):744–746, 1921.
- [4] M. Maheri and R. Adams. On the flexural vibration of timoshenko beams, and the applicability of the analysis to a sandwich configuration. *Journal of Sound and Vibration*, 209(3):419–442, 1998.
- [5] P. Madabhushi-Raman and J. Davalos. Static shear correction factor for laminated rectangular beams. *Composites: Part B*, 27B(285-293), 1996.
- [6] B. Petersson L. Cremer, M. Heckl. *Structure-borne sound: Structural vibrations and sound radiation at audio frequencies*. Springer, Berlin Heidelberg, Germany, 3rd edition, 2005.

eLiQuiD was funded by the EC as a Marie Curie European Industrial Doctorate under Grant Agreement 316422 in the Seventh Framework Programme (FP7) and ran over a period of 4 years (October 2012 – September 2016). The project brought together the Katholieke Universiteit Leuven (KU Leuven) as academic partner, Virtual Vehicle Research Center (ViF) as industrial research centre and the European Automotive Research Partners Association (EARPA) as associated partner and together hosted 4 researchers, drawing together skills and expertise in a range of different technical approaches. ViF and EARPA brought specific applications that embed generic difficulties associated with NVH of electrified vehicles, while KU Leuven brought a diverse range of innovative approaches and the capability of research training, provision of courses and dissemination to the wider community. Together the consortium developed and promoted research, knowledge and application of NVH analysis and design techniques within the EU industry.

Near the end of the 4-year eLiQuiD project, each of the 4 Fellows has written a self-assessment report. This book collects these public domain reports, providing an insight in the theoretical development of each of the approaches studied within eLiQuiD and giving an assessment on their industrial applicability, on open research questions and future challenges. The authors hope that these reports may help others in tackling the substantial challenges still existing in NVH assessment of electrified vehicles.